New vistas for epileptogenic zone (EZ) localization and interpretation

Sheng H Wang[1−4*] Gabriele Arnulfo[5] Lino Nobili[6,7] Vladislav Myrov[2]
Paul Ferrari[8,9] Philippe Ciuciu[3,4] Satu Palva[1,10] J Matias Palva[1,2]

1. Neuroscience Center, Helsinki Institute of Life Science (HiLIEF), University of Helsinki, Finland; 2.Department of Neuroscience and Biomedical Engineering, Aalto University, Finland; 3. CEA, NeuroSpin, France; 4. MIND team, Inria, Université Paris-Saclay, France; 5. Dept. of Informatics, Bioengineering, Robotics and System engineering, University of Genoa, Italy; 6. Child Neuropsychiatry Unit, IRCCS Istituto Giannina Gaslini, member of the European Reference Network EpiCARE, Italy; 7. Department of Neurosciences, Rehabilitation, Ophthalmology, Genetics and Maternal and Children's Sciences, University of Genoa, Italy; 8. Jack H. Miller MEG Center, Helen DeVos Childrens Hospital, USA; 9. Department of Pediatrics and human development, Michigan State University, USA; 10.Centre for Cognitive Neuroimaging, Institute of Neuroscience and Psychology, University of Glasgow, United Kingdom. *sheng.wang@helsinki.fi

Abstract

Drug resistant epilepsy (DRE) accounts for $30-40\%$ of all diagnosed cases of epilepsy. To date, surgical disruption of the epileptogenic zone (EZ) is the most effective treatment for seizure control in DRE. The EZ refers to a pathological brain network that is necessary and sufficient for seizures to emerge. Conventional markers localize EZ inconsistently and incompletely, which leads to only $30-80\%$ of patients achieving long-term seizure freedom after the surgery.

Epileptic seizures are catastrophic events initiated by several abnormal neuronal firing patterns and hypersynchrony from EZ and might spread to other brain areas. We hypothesize that in between seizures, the EZ operates in a dynamical state that mechanistically predisposes it to having seizures. This state leads to aberrant dynamics in spontaneous activity, which can be identified with electrophysiological recordings. To test this idea,we built a generative model for cortical oscillations. When the model was controlled by strong positive feedback, it produced highly bistable oscillations in a critical-like regime of scale-free dynamics. In this regime, we observed anomalies included inhibition-dominance and hyper-irritability, therein a minuscule increase in connectivity can lead to abrupt hypersynchrony onset. Based on these modeling results, we hypothesized that using interictal data in conjunction with the ictal data likely improve EZ-localization.

We retrospectively analyzed the stereo-EEG (SEEG) data from 64 focal DRE patients. Clinical experts identified the "EpiNet" where seizure activity emerged and propagated. We assessed local dynamics and network synchrony using inter-ictal resting-state SEEG from these patient and then used the assessments to train supervised classifiers to identify EpiNet from regions that did not show seizures (NonEpiNet). Combining local and synchrony assessments yielded optimal classification on cohort and individual level. To complement these results, we next conducted unsupervised classification and identified a cohort-level tentative pathological cluster, in which EpiNet and a sizable number of NonEpiNet showed elevated $2-5.4$ Hz synchrony with concurring excessive bistability and inhibition-dominance in $45-225$ Hz oscillations.

Combining all features yielded better EpiNet-classification than using single features (area under the curve reaching 0.85 vs $0.6-0.7$, respectively). This explained why previous studies reported inconsistent EZ-localization with a single marker and also indicated that the aberrant dynamics of EZ indeed have a local and a large-scale aspect. The contacts forming the pathological cluster globally engaged in elevated synchrony and locally showed striking resemblance to our model in the increased seizure risk state. The NonEpiNet from this cluster did not engage in seizures and thus conventionally would have been regarded as healthy. The EpiNet contacts partitioned into the tentative healthy clusters, however, did not bear significant features of aberrant dynamics, and we postulated that these atypical EpiNet contacts could be non-essential to the EZ network required further investigation.

Our findings thus offer novel evidence to support the multi-component hypothesis for EZ, and more future efforts should be directed into investigating the pathological-like NonEpiNet revealed here and with individual specificity and pathological substrates considered.

Highlights

- Brain criticality motivated, novel biomarkers were potent to localize epileptogenic pathology
- Supervised and unsupervised classification were combined to characterize EZ
- Novel evidence was advanced to support the multi-component hypothesis of EZ

Significant statement The Catastrophe theory and Brain Criticality motivated novel physio-markers were tested and found to be effective for classifying the EpiNet with the area under the receiver operating curve reaching 0.85. These novel markers, when combined with phase synchrony features, offered more accurate EpiNet-classification, indicating aberrant local and large-scale physiology collectively reflect the "wholeness" of the EZ pathophysiology. Our results serve a strong proof-of-concept to apply this novel approach to pilot novel clinical utility with both invasive and non-invasive electrophysiological approaches.

Abbreviations
BiS: bistability index
DFA: Detrend fluctuation analysis, the operationalization of LRTCs
E/I: Excitation/inhibition
EpiNet: ictal onset and propagation zone
EZ: epileptogenic zone
fEI: functional excitation-inhibition index
L_{EpiNet}: likelihood of a SEEG contact located in EpiNet.
LRTCs: Long-range temporal correlations
NonEpiNet: not an EpiNet contact
SEEG: stereo-electroencephalography

1 Introduction

Epilepsy is an umbrella term for dozens of diverse syndromes [1] with a common characteristic: an enduring predisposition to having seizures[2]. About 10% of the general population experiences a seizure in their life time, and 4% is diagnosed with epilepsy [3].An epileptic seizure is a surge of hypersynchronous neuronal activity [4] often accompanied by involuntary changes in behaviours and/or subjective experiences [1, 2]. 30–40% epilepsy patients have drug resistant epilepsy (DRE), for whom the most effective way for seizure control is surgically resecting or disconnecting the epileptogenic zone (EZ).

EZ is a pathological network [5] that is necessary and sufficient for initiating seizures, and the disruption of which is sufficient for complete abolition of seizures[6]. Long-term seizure freedom rate in subjects undergone epilepsy surgery varies from low to high values (30–80%) depending on the age of the subject, type of epilepsy, or pathological substrate [7, 8]. In complex cases, such as those submitted to invasive electrophysiological studies, *i.e.,* stereo-electroencephalography (SEEG), seizure freedom is reached in $\sim$ 50% the patients. This suggests that the localization of the EZ is still a challenge in a high percentage of subjects, and a better understanding of individual epileptogenic mechanisms is needed.

In patients underwent SEEG studies, seizures often initiate from and spread to a small number of brain areas [9]. Recent studies have suggested that such epileptogenic brain areas can be characterized by several sustained mechanistic characteristics, such as lesions [10], high gamma oscillations (HFO)[11], spikes [12], concurring pathological slow and fast activity [13], and etc[14]. However, individual markers do not seem to localize EZ consistently across subjects [15, 16, 12]. This evidence

suggests that individual EZ may contain multiple, possibly overlapping components, and some of which may not engage in seizure in complicated cases.

We hypothesized that, irrespective of the seizure types and pathological substrates, the components of the EZ spontaneously express aberrant local and large-scale dynamics (Fig 1a). Because epileptic seizures represent catastrophes, *i.e.*, a sudden regime shift to hypersynchrony [17], in the brain networks, approaches using inter-ictal epileptiform, peri-ictal, or ictal-onset recordings localize the brain regions where the catastrophes emerged. The EZ might also contain areas that do not engage in seizure yet are 'necessary' and 'sufficient' for seizures to emerge and propagate. Hence, to better understand the EZ mechanism, we studied interictal data in conjunction with the seizure onset zone identified with ictal data by clinicians.

The *brain criticality* hypothesis posits that healthy brains operate near a phase transition between asynchrony and synchrony, which is achieved through a balance between excitation and inhibition [18, 19]. From a local perspective, the hallmarks of the criticality include moderate degree of ensemble synchrony (Fig 1 b) with a unimodal distribution, emerging power-law long-range temporal correlations (LRTCs) [20] (bottom panel, Fig 1 **c**), and balanced temporal fluctuations in excitation and inhibition [21]. Contrarily, deviation from criticality has been associated with various brain disorders[22], including not enough synchrony (*i.e.*, sub-critical) in coma [23] and too much synchrony (*i.e.*, super-critical) in epilepsy [24]. In particular, the neuronal activity in epileptic brains has been found to show both super-critical local [25, 26] and network dynamics [24].

The classic criticality assumes a second-order, *smooth* phase transition characterized by a unimodal distribution of synchrony [18, 27]. Nonetheless, canonical models for ensemble firing rate [28] and synchrony [29] also predict *bistability*, *i.e.*,a first-order *discontinuous* phase transition characterized by a bimodal distribution of synchrony (red trace, Fig 1 b). Empirically, bistability is evidenced by animal electrophysiological [30, 31] and human EEG [32, 33] and behaviourally relevant MEG data [34]. Theoretical work has suggested bistability to occur near criticality when influenced by positive feedback [35] or constrained by activity-limiting mechanisms due to over-excitation [36]. High degree of bistability has long been suggested as a universal indicator of catastrophes [17] (Supplementary Fig1) in various complex systems (reviewed in [34]). This idea previously motivated us to consider seizures as neuronal catastrophes, and we trialed and found neuronal bistability to be a potent marker for regions engage in seizure[34].

From a large-scale perspective [37], synchrony between ensembles is thought to be instrumental for establishing neuronal communications [38, 39] and synchrony level is moderate at criticality in healthy adults [40]. On the other hand, anomalies in synchrony are associated with brain disorders [41]. Recent SEEG studies suggested that during inter-ictal periods, pathological regions are more inhibited [42] and synchronized presumably preventing seizures, whereas this control diminished before seizure onset [43, 5]. To study the relationship between synchrony and criticality in DRE, we obtained narrow-band phase synchrony *connectome*[44], *e.g.*, a connectome was treated as a *graph* wherein contacts were *nodes* [45]. If resting-state hypersensitivity in EZ was indeed the case, the constituents of EZ should show elevated 1st- and 2nd-order centrality (Fig 1d) [46], *i.e.*, a node's connectivity and its functional neighbours' connectivity, respectively. Combining abnormal synchrony features and aberrant criticality should better characterize EZ.

Epilepsy is a disease of the brain networks [47, 5], and therefore to better localize EZ, **the emergent pathophysiology of EZ should be investigated simultaneously on local and network level.** To achieve this comprehensive EZ-localization, we proposed here a unique approach that combines several state-of-the-art local and network biomarkers with advanced classification methods. We retrospectively tested this approach on 64 DRE patients. The regions where seizure initiated and propagated (EpiNet) were identified with conventional clinical approach. To identify EpiNet with our approach, we first assessed criticality and synchrony from ictal-free resting-state SEEG, which were then used as features to train supervised classifiers for EpiNet in individual patients. As data-driven identification of EpiNet to complement the supervised classification, we employed unsupervised classifiers to characterize the pathological profiles. This allows us to localize within individuals, the contacts

that showed aberrant criticality and elevated synchrony as the EpiNet.

2 Methods and material

2.1 Subjects and SEEG recording

The SEEG recordings were conducted at the Niguarda "Ca' Granda" Hospital, Milan, Italy. We selected a subset of 64 DRE patients (mean±std age: 29.7±9.5 years, 29 biological females, more details see S.Table 1) from a large cohort [7] who: ***i)*** were the first time to undergo the SEEG procedure; and ***ii)*** had no previous brain surgeries, and ***iii)*** were free of cognitive impairment and psychological or neurological conditions, and ***iv)*** had been diagnosed with focal onset seizures. 9 subjects had less than 5 seizure onset and propagation zone (EpiNet) or non-EpiNet (NonEpiNet) contacts were excluded from the EpiNet-classification analyses. 45 subjects underwent surgery or radio-frequency thermo-coagulation (RF-TC) [9]. In line with [7], a patient's cumulative surgical outcome with a minimum follow-up of 24 months is considered as 'favourable' when meeting the criteria of International League Against Epilepsy (ILAE) classes 1 and 2 (corresponding to Engel classes Ia–Ic). The outcome is considered as "unfavourable" when a patient was not free of disabling seizures (ILAE classes 3–6, Engel classes II–IV).

We obtained 10-min of resting-state recording as monopolar local-field potentials (LFPs) with shared reference in the white-matter away from the EpiNet locations[48]. These resting-state data were ictal-free, and there were no seizures one hour prior to or after the recording. All patients were under anti-seizure medication with a large variability in the compounds and dosage (See Suppl. Table 1), and the recording time from the last drug adminstration were not controlled. Therefore, studying the drug effects were not considered. We used platinum-iridium, multi-lead electrodes (DIXI medical, Besancon, France), each of which has 8 to 15 SEEG contacts that were 2 mm long, 0.8 mm thick and had an inter-contact border-to-border distance of 1.5 mm. The Freesurfer software [49] was used for extracting cortical parcels from pre-surgically obtained T1 MRI 3D-FFE. An automated SEEG contact localization method was then used to assign each SEEG contact to a cortical parcel with sub-millimeter accuracy [50].

Before electrode implantation, all patients gave written informed consent for participation in research studies and for publication of data. This study was approved by the ethical committee (ID 939) of the Niguarda Hospital, Milan, Italy, and was performed according to the Declaration of Helsinki.

2.2 Identifying seizure onset and propagation zone (EpiNet)

Prior to surgery, clinical experts identified SEEG contacts located in the EpiNet by visual analysis of the SEEG traces, and each procedure was carried out by one expert and validated by another [9]. Various peri-ictal and ictal events may initiate from the seizure onset zone (SOZ), including low-voltage fast discharge, spike-and-wave, and poly-spike slow bursts, etc [4]. The brain areas inside the seizure propagation zone (SPZ) do not initialize ictals and often show delayed, rhythmic modifications after seizure initiation from SOZ [5, 51]. It is also common to see some SEEG contacts to have been identified as SOZ and SPZ simultaneously (SOPZ). In this study, we refer to SOZ, SPZ, and SOPZ collectively as the **EpiNet**. The EZ is a diseased brain network [5, 51] that may have multiple partially overlapping components such as the structural lesions, high gamma oscillators, and irritative zone, and some of these components may not engage in seizure [14, 52]. Therefore, some the brain areas that did not engage in seizures (**NonEpiNet**) could also be a part of the EZ.

2.3 Preprocessing and filtering

Contacts located in EpiNet are known to occasionally pick up inter-ictal events (IIE) characterized by high-amplitude spikes with widespread spatial diffusion, which could bias criticality estimates [26].

We followed approach used in [53] to identify and exclude IIEs from biasing the analyses. Briefly, each contact broad-band signal was first partitioned into non-overlapping 500 ms segments; a segment was tagged as 'spiky' and discarded from LRTCs and bistability analyses when at least 3 consecutive samples exceeding 7 times the standard deviation above the channel mean amplitude. Last, narrow-band frequency amplitude time series was obtained by convoluting the broad-band SEEG contact time series with Morlet wavelets (m=5) from 2 to 225 Hz with equal inter-frequency distance on log_{10} scale.

2.4 Assessing criticality in local neuronal oscillations

The criticality assessments for narrow-band neuronal oscillations are briefly described as follow (the formal definitions and exemplary data can be found in the Supplementary Methods).

- The critical exponent obtained using linear detrend fluctuation analysis (DFA) is conventionally used to assess the LRTCs of a neuronal oscillation [20]. $DFA = 0.5$ indicates that the time series is indistinguishable from a random walk process with no long-range memory; $0.5 < DFA < 1$ indicates significant LRTCs, *i.e.*, an indication of criticality; $1 < DFA < 2$ indicates the time series is non-stationary.

- The BiS index quantifies the degree of bistability of a narrow-band neuronal oscillation [32]. First, the empirically observed probability distribution of the narrow-band power time series is fitted with a single exponential and a bi-exponential model. Then, the BiS is derived from the model comparison between the two competing models based on Bayesian information criterion. $BiS > 3$ indicates bistability, otherwise unimodal.

- The functional excitation-inhibition index (fEI) assesses the temporal fluctuation in excitation-inhibition of a neuronal oscillation [21]. $0 < fEI < 1$ indicates that the oscillation demonstrated inhibition-dominated temporal dynamics; $1 < fEI < 2$ indicates excitation-dominated dynamics; and $fEI = 1$ with a constraint of $0.5 < DFA < 1$ indicates an excitation-inhibition balanced dynamics.

2.5 Assessing and validating phase synchrony derivatives

We utilized all-to-all functional connectivity estimated for the same cohort from our recent publication [53]. The connectivity were individual subject phase synchrony matrices estimated using the phase-locking value (PLV) for 50 narrow-band frequency time series (Morlet wavelets, $m = 7.5$) covering 2–450 Hz with equal inter-frequency distance on log_{10} scale.

The narrow-band PLV matrices were collapsing into 1D synchrony derivatives (synch.D) to characterize individual contact connectivity [46] using the Brain Connectivity toolbox (brain-connectivity-toolbox.net). We estimated first-order synchrony derivatives, *i.e.*, the connectivity of a given contact, with *effective weight* (We) and *eigenvector centrality* (EVC). We is the linear aggregating available edges. EVC is a self-referential measure of centrality, *e.g.*, nodes have high EVC if they connect to other nodes that have high EVC. We estimated second-order synchrony derivatives, *i.e.*, the connectivity of the neighbours of a given contact, with *clustering coefficient* (Cc) and *local efficiency* (LE). Cc is the fraction of node's neighbors that are neighbors of each other. The *efficiency* is defined as the average inverse shortest path length in the network, and LE is the *efficiency* assessed in the neighborhood of a node n_i, *i.e.*, all the nodes connected to n_i.

Due to the inhomogeneity of SEEG spatial sampling and the deletion of edges between contacts sharing the same white-matter reference channel (recommended by [48]) , we ascertained the validity of the synchrony derivatives with two different sets of simulations. First, for each subject's narrow-band PLV matrices, random edge deletion was used to emulate the removal of interactions between contacts that shared the same white-matter contacts. Second, node deletion was used to emulate the individual variability in spatial sampling and therefore possible sub-sampling. All these synchrony derivatives were consistently robust against simulated random deletion (Supplementary Fig 6).

2.6 Normalizing, frequency clustering, and differentiating neuronal features

We first differentiated contacts recorded from EpiNet and NonEpiNet within subjects and then aimed to train cohort-level models for supervised EpiNet-classification. The criticality and phase synchrony estimates were known to show co-variability and considerably large individual variability across subjects [40]. Therefore, we normalized the criticality and synchrony derivatives as: $\hat{x}_i = (x_i - median(X))./max(x_i - median(X))$, where, X is a 1D vector of criticality or synchrony derivative for a given frequency within a subject (Fig 3 a–f).

Because the topological features of narrow-band criticality assessments were similar between neighbouring frequencies and different between fast and slow brain rhythms, twenty narrow-band criticality assessments were next collapsed into four frequency clusters based on observed similarity as δ (2–4 Hz), $\theta - \alpha$ (5.4–11 Hz), β (15–30 Hz), and $\gamma_{1,2}$ (45–225 Hz) (Supplementary Fig 6); Likewise, as we previously reported that the narrow-band PLV matrices showed topological similarity [53], fifty narrow-band synchrony derivatives were collapsed into six frequency clusters as: $\delta - \theta$ (2–5.4Hz), α (6.1–13 Hz), β (15–30 Hz), γ_1 (40–96 Hz), γ_2 (110–250 Hz), and γ_3 (270–450 Hz) ([53]).

Subsequently, the effect size of differences between EpiNet and NonEpiNet in these normalized and frequency clustered feature data were assessed with Cohen's d and compared with the 99%-tile of Cohen's d observed from 1,000 EpiNet-NonEpiNet label-shuffled surrogates (Fig 3 g–h).

2.7 Supervised EpiNet-classification using the random-forest

We first assessed the individual feature importance and then conducted supervised EpiNet-classification using the EpiNet labels identified by the clinical experts. The feature importance of these neuronal estimates were assessed with the SHapley Additive exPlanations (SHAP) values [54]. The SHAP values is a generic metric to explain any tree-based model by explicating the local and global interpretability of features, which advances the transparency that conventional "black-box" classifications approaches lack of. The non-parametric random-forest method was employed for supervised EpiNet-classification [55]. The random-forest algorithm is a machine learning method uses bootstrapped training data and combines the simplicity of decision trees with extended flexibility to handle new data.

2.8 Unsupervised classification by contact cluster analysis

We also conducted unsupervised contact classification by cohort level contact cluster analysis, *i.e.*, without considering any human inputs as the ground truth for pathophysiology. This was done by first pooling all feature data of the whole EpiNet-classification cohort (contacts $\times$ features, 2D scalars), then computing all-to-all feature-similarity (*i.e.*, Spearman's rank correlations r) between contacts (Fig4e), and last conducting clustering analyses using the unweighted pair group method with arithmetic mean (UPGMA) [56]. The UPGMA is an agglomerative hierarchical clustering approach that builds a hierarchical tree through an iterative procedure to reflect the distance between all pairs of objects (*i.e.*, either a contact or a cluster of contacts) represented by the similarity matrix. The information about distance tree structure is then used to partition the data into well delineated clusters.

3 Results

3.1 Cortical oscillation model: strong positive feedback was associated with high bistability and increased seizure risk

To investigate the link between neuronal bistability, criticality, and the emergence of seizure-like hypersynchrony, we built a modified Kuramoto model based on our recent work [34]. The Kuramoto model is simple model for generating ensemble synchrony dynamics (Supplementary eq.3), and the **order** parameter (R) quantifies the ensemble synchrony (*e.g.*, $R \to 0$ and $R \to 1$ indicate no synchrony and full synchrony, respectively, Supplementary eq.6). Bistability means abrupt switching between an ON and an OFF mode in order during the period of observation. In line with the canonical cusp catastrophe prediction [17], we expected that, as the model order is influenced by neuronal coupling (a) and

local positive feedback (b), bistability should emerge when b intensifies (Supplementary Fig 1 and eq.1).

We assessed bistability with BiS, LRTCs with DFA, the excitation/inhibition balance with fEI for the model order time series. At low level of positive feedback, power-law scaling LRTCs emerged at low to moderate levels of order (Fig 1e) (Supplementary Fig 2) – indicating a smooth phase transition between asynchrony and synchrony as predicted by the classic criticality hypothesis. However, when influenced by a strong positive feedback, the model became unstable and hyper-sensitive to minuscule increments in coupling (Δa_2 in Fig 1e) to demonstrate seizure-like hypersynchrony. Interestingly, from the high bistable regime, Δa_2 in fact drove the model from an inhibition-dominant, abruptly through an excitation-dominant critical-like regime, into a super-critical regime of hypersynchrony (Fig 1f).

These novel *in silico* results thus confirm the cusp catastrophe prediction and further suggest that concurrent inhibition-dominance and excessive bistability – in a critical like regime – characterize an increased seizure risk.

3.2 SEEG Resting-state: EpiNet showed high bistability and elevated large-scale phase synchrony

Clinical experts identified the seizure onset and propagation zones (EpiNet) in each patient (n=64). We assessed local criticality and large-scale phase synchrony for 10-min of SEEG ictal-free resting-state data and examined whether these assessments could differentiate EpiNet from the regions that did not engage in seizures (NonEpiNet).

The amplitude envelope of neuronal oscillations is equivalent to the model synchrony, and local criticality of the narrow-band SEEG data was assessed in the same manner as for the model. In a recent publication, we assessed all-to-all phase synchrony with the phase locking value (PLV) for the same cohort [53]. These PLV data were reused here to obtained the first- and second-order synchrony derivatives (Methods). Before analyses, we ascertained the robustness of these synchrony derivatives by a large number of simulations across all subjects (Methods and Supplementary Fig 4).

Visual inspection of individual data readily revealed differences between EpiNet and nEpiNet contacts. For example, an EpiNet and a nearby NonEpiNet contact from the frontal area of subject X demonstrated clear contrast in traces (Fig2 **a**–**b**) and the criticality assessment (Fig2 **c**–**d**) and $4HzPLV$ synchrony (Fig2 **e**–**f**). In this subject, the EpiNet contacts showed elevated bistability and LRTCs from 20 to 200 Hz (Fig2 **g**) oscillations and more pronounced synchrony from 2 to 20 Hz oscillations (Fig2 **h**). Additionally, it was also possible to observe elevated bistability in NonEpiNet contacts in some subjects (Supplementary Fig 3 c).

On the cohort level, oscillation amplitude decayed as frequency increased with individual variability in 2–20 Hz frequency band (Fig 3**a**). Pooling all contacts from all subjects revealed that criticality and synchrony derivatives both showed frequency-specific differentiating effects for EpiNet and nEpiNet. EpiNet showed elevated bistability and inhibition-dominance in 45–225 Hz and 15–30 Hz (Fig 3**b, c**), and DFA showed a relatively weak effect (Fig 3**d**). Meanwhile, EpiNet showed elevated first- and second-order synchrony derivatives (Fig 3**b, c**, respectively).

Overall, narrow-band data showed anatomical similarity between neighbouring bands but dissimilarity between distinct bands of frequencies (Supplementary Methods). To improve interpretability, we next clustered these narrow-band data into few band-collapsed data and tested for differences between EpiNet and NonEpiNet. Briefly, 20 narrow-band criticality maps were collapsed into four bands (defined on top of Fig 3**b**–**d**, see also Supplementary Fig 6). Based on the topological similarity reported in ([53]), 50 narrow-band synchrony derivative maps were collapsed into six bands (indicated on top of Fig 3**e, f**).

To summarize, EpiNet showed excessive local bistability with concurrent inhibition-dominance most prominently in $\gamma_{1,2}$ ($40-225$ Hz) followed by β ($15-30$ Hz) band oscillations (Fig 3**g**). These aberrant criticality in the fast rhythms were in line with the model prediction (Fig 1**f**). Furthermore, EpiNet

contacts showed simultaneously elevated first- and second-order synchrony derivatives in $\delta - \theta$ ($2 - 5.4$ Hz) followed by γ_1 ($40 - 96$ Hz) band (Fig 3**h**). This indicted that EpiNet were central nodes (Type-1 node, Fig 1**d**) characterized by elevated resting connectivity to EpiNet and between the functional neighours of EpiNet.

3.3 Supervised EpiNet classification: combining local criticality and synchrony assessments yielded the best outcome

Next we asked if criticality and synchrony derivatives could classify EpiNet for individual patients and thus hold value for clinical utility. This was done in three steps: first, we assessed the similarity between criticality and synchrony derivatives; next, as a proof-of-concept for individual EpiNet-classification, we conducted a population level cross-validation using the random forest algorithm, a supervised Bayesian classifier [55]; last, we conducted individual EpiNet-classification.

First, we inspected feature similarity by computing Spearman's correlation between band-collapsed local criticality and connectivity estimates across all contacts (Supplementary methods). As we previously reported [34], DFA and BiS were positively correlated between all bands (Fig 4**a**, respectively). Importantly, BiS and fEI were negatively correlated which constituted the first empirical evidence of concurring bistability and inhibition-dominance in EpiNet to support the model prediction (Fig 1**e**–**f**). The weak correlation between criticality and connectivity (Fig 4**b**) implied that they reflected non-overlapping physiological features. However, both feature families showed differentiating effects for EpiNet (Fig 3), we predicted that combining them would likely offer better EpiNet-classification, *e.g.*, than using either of them alone.

As a precaution, we next took two additional procedures to validate that criticality and synchrony assessments represented useful features for EpiNet-classification. First, we assessed global and within-subject feature importance with the Shapley Additive exPlanations (SHAP) values for the random-forest classifier [54]. This revealed that, on the population level, γ band BiS and fEI, β band BiS, and $\delta - \theta$ band LE were among the most important individual features (Supplementary Fig 7). Next, we conducted a population level cross-validation with $1,000$ independent iterations, each of which was a random $80 : 20\%$-partition (training:test set) (Supplementary methods). We tested EpiNet-classification using criticality alone, synchrony derivatives alone, and combining criticality and connectivity and for "cortical contacts only" and "all contacts" (*i.e.*, cortical and subcortical). These systematic tests revealed that combining criticality and connectivity ('All' in Fig 4c) yielded the best classification result with the area under curve (AUC) of the receiver operating characteristic reaching 0.85 ± 0.002 (mean $\pm$ std). These results thus offered the proof-of-concept for within-patient EpiNet-classification.

Last, we conducted within-patient EpiNet-classification with leave-one-out validation (n=55 patients) so that each patient's SEEG contacts constituted the test set and the contacts from all other patients as training set. Using all features yielded the best result with a mean AUC of 0.73 ± 0.16 for all contacts, and 0.72 ± 0.16 for cortical contacts only (Fig 4**d**), with no difference between whether or not including subcortical contacts (repeated t-test, $p > 0.55$). Interestingly, synchrony derivatives were more potent than criticality for EpiNet-classification in population cross-validation (Fig 4**c**), whereas criticality represented more potent features than connectivity in within-patients classification (Fig 4**d**).

3.4 Unsupervised classification: some NonEpiNet were pathological-like and some EpiNet were atypical

EZ represents a pathological brain network that is sufficient and necessary for generating seizures. The EZ might comprise of multiple functional components and not necessarily all of them would engage in seizures [14]. Hence, we asked whether the current dataset contained brain areas bearing the pathological features similar to EpiNet but did not engage in seizures, *i.e.*, the pathological-like NonEpiNet. To answer this question, we adopted an unsupervised classification approach.

We first estimated all-to-all feature similarity between contacts of the whole cohort and then conducted clustering analyses of this contact similarity matrix (Supplementary methods). Thereby, contacts belonging to the same cluster are more similar with each other than with the contacts from other clusters. We examined whether there were well-defined clusters in the similarity matrix and found that through a range of partitioning resolutions, three clusters remained stable in their constituent contacts and were representative of the whole cohort (Supplementary Fig 8 **a**–**b**). Thus, we chose the 3-cluster partition solution for further analyses (cluster size $n = 2730, 1378, 1243$, respectively) (Fig 4e).

We then asked whether the clusters represent distinct (patho-)physiological profiles by joint analyses of the clustering and within-patient EpiNet-classification. Based on the model trained with the cohort feature data, the classifier assigned each contact an EpiNet-likelihood ($L_{EpiNet}, 0-1$) to indicate how likely it was an EpiNet. The Cluster-1 contacts (pink, Fig4 **f**) showed larger mean L_{EpiNet} than Cluster-0 and -2 (unpaired t-test $-log_{10}(p) > 10^{15}$ and > 234.2 , respectively), whereas there was no difference between cluster-0 and -2 (unpaired t-test, $-log_{10}(p) < 0.35$). Here, a larger L_{EpiNet} indicated that pathological-like contacts were indeed more concentrated in Cluster-1 (in-cluster EpiNet:NonEpiNet $= 48.8\% : 51.2\%$). The probability of observing EpiNet in Cluster-1 (48.8%) were more than twice larger than that of Cluster-1 and -2 (23.0% and 21.2%, respectively), which further supported that Cluster-1 represented pathophysiology.

We next asked what features characterized the three contact clusters by comparing criticality and synchrony assessments between clusters. Cluster-1 showed elevated local efficiency (Fig 4**i**) and eigen vector centrality (Supplementary) most prominently in $\delta - \theta$ and γ_1 band. The concurrent larger first- and second-order synchrony derivatives suggested that these brain areas were relatively central (Type-1 node in G3, Fig 1**f**). Cluster-1 also showed elevated bistability (Fig4**j**) with concurring inhibition-dominance (Fig4**k**) in $\gamma_{1,2}$ and β band comparing to Cluster-0 and -2. Last, Cluster-1 showed higher DFA in $\gamma_{1,2}$ band (Fig4**l**).

Notably, in the tentatively pathological Cluster-1, 25.2% of NonEpiNet contacts had L_{EpiNet} greater than 50% (Fig 4g). Hence, the the ratio of such 'pathological-like' NonEpiNet contacts ($p_{NonEpiNet-clust1}$) in a patient might tell the extent of the EZ network that could not be detected using conventional approaches. The $p_{NonEpiNet-clust1}$ was marginally higher in patients with predominantly frontal EpiNet ($4.7 \pm 3.8\%$, $n = 15$) than the patients with EpiNet in temporal or other lobes ($2.6 \pm 2.6\%$, $n = 40$) (unpaired t-test, $p < 0.018$), whereas the mean L_{EpiNet} of all NonEpiNet contacts in the frontal-EpiNet patients ($23.6 \pm 4.9\%$, $n = 15$) and other patients ($24.5 \pm 7.1\%$, $n = 40$) had no difference (unpaired t-test, $p > 0.667$). This suggested that these tentatively pathological NonEpiNet were not detected during conventional pre-surgical EZ mapping in the patients with frontal lobe seizure, who have previously been suggested to represent a special type of epilepsy [57].

Last, $p_{NonEpiNet-clust1}$ did not predict surgical outcome (favourable: $2.9 \pm 3.1\%, n = 26$ vs unfavourable: $3.9 \pm 3\%, n = 19$, unpaired t-test, $p > 0.283$) (statistical tests and p values are detailed in Supplementary).

4 Discussion

We showed with computer modelling that strong positive feedback led to excessive bistability in neuronal oscillation amplitudes, functional inhibition dominance, and lowered seizure threshold. The SEEG analyses revealed that EpiNet contacts showed higher bistability, more inhibition dominance, and elevated large-scale phase synchrony comparing to NonEpiNet contacts. In the supervised EpiNet-classification, combining local criticality and synchrony assessments yielded most accurate results within individual patients. Cohort level unsupervised classification discovered that some NonEpiNet contacts − although did not engage in seizures − showed the same pathophysiological patterns as the EpiNet. The *in silico* and *in vivo* analyses converged on to the conclusion that epileptogenic pathophysiology can be characterized as high bistability and inhibition dominance in the fast brain rhythms ($45 - 225Hz$) with concurring stronger long-range temporal correlations and network phase synchrony in the slow rhythms ($2 - 5.4Hz$).

4.1 Excessive neuronal bistability and elevated synchrony indicate seizure risks

Our simulations showed that a neuronal ensemble can be driven into a seizure-like hypersynchrony phase in both unimodal and bistable critical-like dynamical regimes. However, we highlighted that, in the model, strong local positive feedback led to a high bistability regime of neuronal oscillations, in which we observed a drastically reduced threshold to seizure-like hypersynchrony. The positive local feedback in this model can be generalized as a self-facilitation mechanism that is thought to universally lead to bistability in complex systems irrespective of their physical details [35]. In particular, excessive bistability represents a first-order discontinuity with harmful hysteresis (reviewed in [34]) and phenomenologically a signature of incoming catastrophic events [17, 58].

Theoretically, in large-scale brain networks, self-facilitation could be associated with high resource demand and/or depletion of resource and ensuing bistable neuronal avalanche dynamics [36]. Likewise in local models, *e.g.*, the classic Wilson-Cowan model, strong E-to-E positive feedback between excitatory cells and E-to-I disinhibitory connectivity can lead to local bistable firing rates [28, 59]. Unchecked local E/I balance obvious could lead to high resource demand and/or depletion in a local neuronal populations. In general, high resource cost components of the brain networks may be particularly vulnerable to abnormal development or pathological attack, resulting in various disorders [41]. These examples of self-facilitation in large-scale and local models are in line with recent suggestions of the positive feedback loop between seizure activity and metabolic anomalies such as glucose dysregulation [60, 61] or neuroinflammation [62, 63].

4.2 Not all of the brain regions exhibited EpiNet-like pathophysiology engaged in ictal activity

The unsupervised classification revealed a pathological-like contact cluster with the in-cluster EpiNet : NonEpiNet ratio of 48.8% : 51.2%. The NonEpiNet in this cluster did not engage in seizure throughout the whole inpatient SEEG monitoring period (ranging from several days to weeks) and therefore would have been identified as "non-pathological" according to the current conventions. However, these NonEpiNet contacts in only 10-min of resting-state SEEG readily exhibited similar dynamics like the EpiNet as they both spontaneously engaged in elevated phase synchrony while locally showed striking resemblance to the model inside the high bistability regime. This implies that the EZ network might be comprised of brain areas do not actively engage in seizures.

On the other hand, some EpiNet contacts were partitioned into the other two clusters that did not bear significant similarity to the pathophysiology predicted by our model and were not as central in the $\delta-\theta$ band synchrony as the pathological-like cluster. We postulated these atypical EpiNet contacts might be non-essential to the EZ network (*i.e.*, Type-2 nodes in Fig 1)**d**.

More future efforts should be directed into elucidating the interesting dissociation revealed here, especially the functional role of the pathological-like NonEpiNet areas during rest [14] and their relationship to the functional networks in other brain states [64].

4.3 The EZ is a diseased brain network with localized pathologies

Epilepsy is an umbrella condition encompassing dozens of complicated seizure types [1] with various pathological substrates and several hundreds of identified genetic correlations [2]. It is unclear but highly likely that seemingly identical pathophysiological and behavioral symptoms are caused by different underlying neurophysiological or biological pathology; likewise, identical underlying pathological substrate might produce categorically different pathophysiological and behavioral expressions across patients and in the same patient across different cycles [65]. In individual brains, the epileptic seizures may be triggered by various risk factors with a wide range of underlying pathological substrates [2], yet the epileptogenic dynamics likely obey few and simple rules, *i.e.*, bifurcation mechanisms [66]. Hence, categorizing epileptogenic mechanisms by local and network pathophysiological feature may shed new lights on the difficult problem of understanding individual epileptogenic mechanisms.

The EZ is a diseased brain network [5, 51, 67] that could comprise of several functional components with distinct features, *e.g.*, EpiNet, structural lesions, high gamma oscillators, and irritative zone, etc [14, 52], and some components could have a varying degree of functional overlapping across individuals. This might be the reason for why individual markers often localize EZ inconsistently across subjects [15, 16]. Our SEEG analyses (Fig $3-4$) revealed that the pathological brain networks in the current focal onset DRE cohort were characterized by strong phase synchrony, and localized highly bistable, and inhibition-dominant neuronal populations. These results thus offered convincing evidence support to the "concurrent local and global pathology" hypothesis.

4.4 A comprehensive EZ-localization approach needs further testing

To address the multi-component hypothesis for EZ, we took a comprehensive approach by evaluating the feature importance (Supplementary Fig 7) and flexibly allowing for the assessment and commission of several important neurophysiological features to supervised and unsupervised classifiers for individual EZ-localization. In this study, the clinical experts identified the EpiNet case by case based on the SEEG readouts during several days of inpatient monitoring (Methods). We assessed neurophysiological features from 10-min of ictal free resting-state SEEG and used the EpiNet as the "ground truth" (hence supervised) for training cohort level models to classify pathological areas in individual brains. The supervised classification yielded overall accurate individual EpiNet classification results, albeit with individual variability.

However, the EpiNet could still be an imperfect "ground truth" for EZ pathophysiology for two reasons. First, whether there are sub-types of EpiNet and/or the overlap of the EpiNet with other functional units of the EZ are still unclear. Second, EpiNet identification accuracy could be variable across subjects because the spatio-temporal signatures of ictal events may vary [4] and sometimes can be ambiguous in different seizure types [68] and temporally dependent on multiday fluctuations of seizure risk [69] or individual seizure cycles[65]. In future efforts, these factors should be investigated with individual etiology and surgical outcome considered – ideally in conjunction with other high resolution imaging modality such as video-EEG, MEG, and fMRI.

5 Conclusion

We showed that, in this cohort of focal onset DRE patients, combining features of ongoing local criticality and large-scale connectivity has a tremendous potential for comprehensive EZ-localization. More future efforts should be directed into investigating the NonEpiNet with pathological features revealed here – ideally in larger cohorts with more seizure types and pathological substrates included.

6 Acknowledgements

7 Funding

This project was funded by: the Academy of Finland grant (SA 253130 and 296304) awarded to JMP; Sigrid Jusélius Foundation grant awarded to SP and JMP; NEXTGENERATIONEU (NGEU) and by the Ministry of University and Research (MUR), National Recovery and Resilience Plan (NRRP), project MNESYS (PE0000006) – A Multiscale integrated approach to the study of the nervous system in health and disease (DN. 1553 11.10.2022) awarded to LN; the theoretical work was partially funded the Ella and Georg Ehrnrooth Foundation awarded to SHW (14-10553-2); the analytical tools development, data analyses, and publication preparation have been been supported by the Finnish Cultural Foundation postdoc fellowship (00220071) and the Sigrid Jusélius Foundation fellowship (210527) granted to SHW. We are grateful for the financial support.

8 Figures

8.1 Fig 1

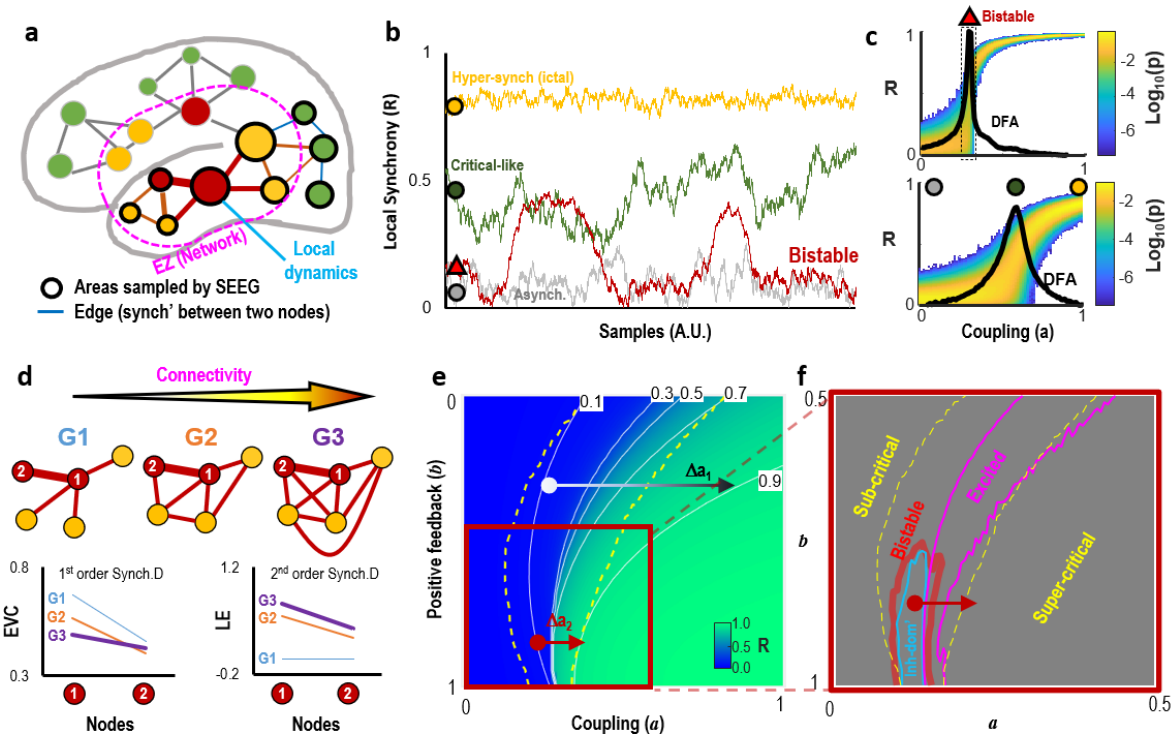

Figure 1: **Hypothesis: aberrant local criticality and elevated large-scale synchrony concurrently characterize spontaneous activity of EZ. a.** A generalization of the multi-component hypothesis [14] for EZ pathoneurophysiology: the EZ (magenta) may comprise of brain areas that engage in seizures (EpiNet, red) and those do not (NonEpiNet, yellow). SEEG sampling variability: not all areas of EZ were sampled, and some healthy areas (green) were also sampled. **b.** Exemplary R time series when the model ensemble is in sub-critical (grey), critical-like (green), super-critical (orange), and bistable (red) phase.Real part (the oscillation) were omitted to avoid crowding. **c.** The tuning of probability distribution (color map) and DFA (black line) of R as the model in strong (top) and weak local positive feedback (bottom); the corresponding time series in different phases were shown in **(b)**; DFA: critical exponents of LRTCs. **d.** A toy network model: the 1st- and 2nd-order synchrony derivative (Synch.D, see Methods) of Type 1 (central) node are consistently larger than that of Type 2 (peripheral) node as connectivity increases; EVC: eigen vector centrality is a 1st-order metric quantifying the connectivity of a node to the whole network; LE: local efficiency is a 2nd-order metric quantifying the connectivity between the neighbours of a node. **e–f.** Local criticality assessed from spontaneous activity of the model. **e.** Mean R as a function of a and b; the enclave within yellow dashed lines is the critical-like regime ($DFA > 0.6$); Δa_1 and Δa_2 indicate required increment in a at low and high level of b, respectively, to drive the model from critical to super-critical state, *i.e.*, seizure-like activity. The y axis is reversed to be comparable with the cusp fold (Supplementary Fig 1). **f.** Association between criticality, bistability, inhibition-dominance, and excitation-dominance (enclaves inside red, cyan, and magenta, respectively).

8.2 Fig 2

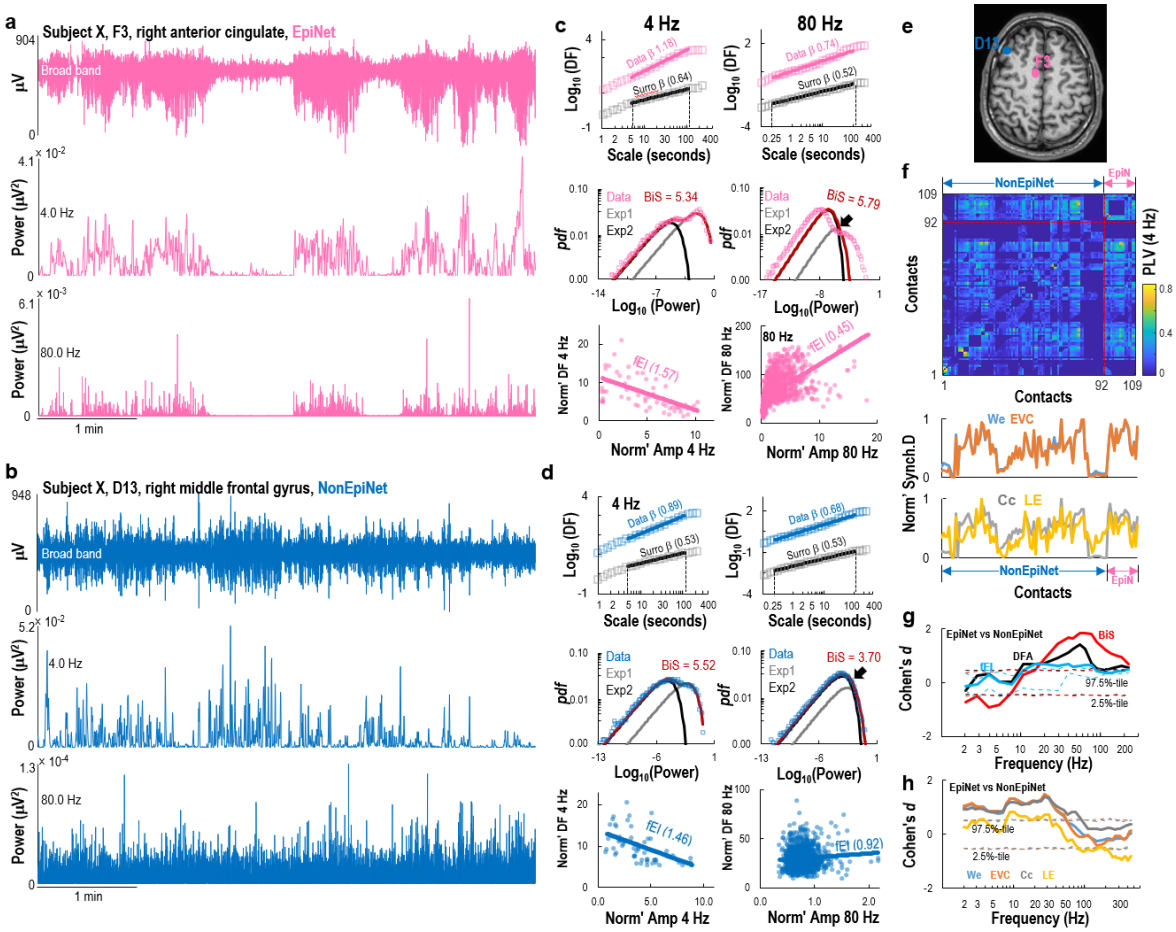

Figure 2: **Evidence of individual level differences between EpiNet and NonEpiNet. a–b**. Five minutes of broad-band and narrow-band traces from **(a)** an EpiNet contact and **(b)** a NonEpiNet contact from one subject X. **c.**Top: the fitting for DFA exponent (β), middle: BiS index, and bottom fEI index for 4 Hz and 80 Hz traces from **(a)**. Markers and solid lines indicate observed data and fitted models, respectively. **d.** The same for **(b)**. **e.** SEEG contact locations of subject X. **f.** Top: X's 4 Hz phase-locking value (PLV) adjacency sorted by EpiNet and NonEpiNet contacts; bottom: normalized synchrony derivatives of the SEEG contacts. We: effective weight; EVC: eigen vector centrality; Cc: clustering coefficient; LE: local efficiency. **g–h** Difference between EpiNet and NonEpiNet contacts in **(g)** criticality assessments and **(h)** synchrony derivatives. Dashed line indicate 2.5% and 97.5%-tile observed from 1,000 label shuffled surrogate data.

8.3 Fig 3

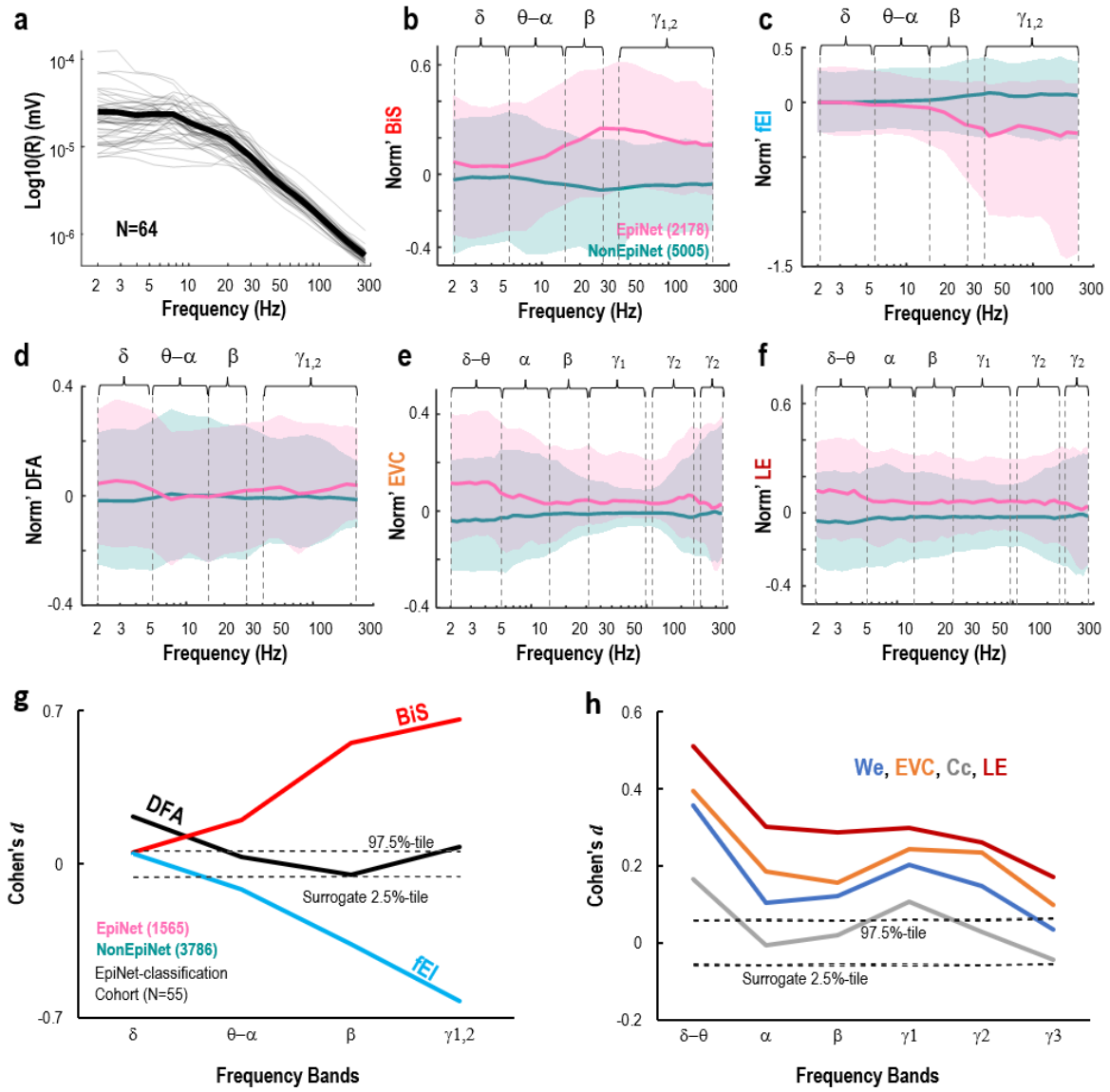

Figure 3: **Ictal onset and propagation zone (EpiNet) showed anomalies concurrently in neuronal criticality and connectivity.** **a–f**. Demographics of the whole cohort (N=64). **a.** With-subject (thin) mean SEEG amplitude and group average (thick). **b–f.** Normalized narrow-band frequency criticality and synchrony derivatives. **b.** Mean eigen vector centrality (first order). **c.** Mean local efficiency (second-order). **d.** Mean bistability index. **e.** Mean functional excitation and inhibition balance index. **f.** Mean power-law exponents obtained from detrend fluctuation analysis. In **(b–f)** shades indicate 25 and 75%-tile of observed data; frequency clusters of criticality: δ (2–4 Hz), $\theta - \alpha$ (5.4–11 Hz), β (15–30 Hz), and $\gamma_{1,2}$ (45–225 Hz); frequency clusters of synchrony derivatives: $\delta - \theta$ (2–5.4Hz), α (6.1–13 Hz), β (15–30 Hz), γ_1 (40–96 Hz), γ_2 (110–250 Hz), and γ_3 (270–450 Hz). **g–h.** Differences between EpiNet and NonEpiNet in band clustered metrics for the EpiNet-classification sub-cohort (N=55). **g.** Differences in local criticality. **h.** Differences in synchrony derivatives. Dished lines in (**g–h**) indicate observed confidence interval from 10^4 label-shuffled surrogates conducted independently for each metric.

8.4 Fig 4

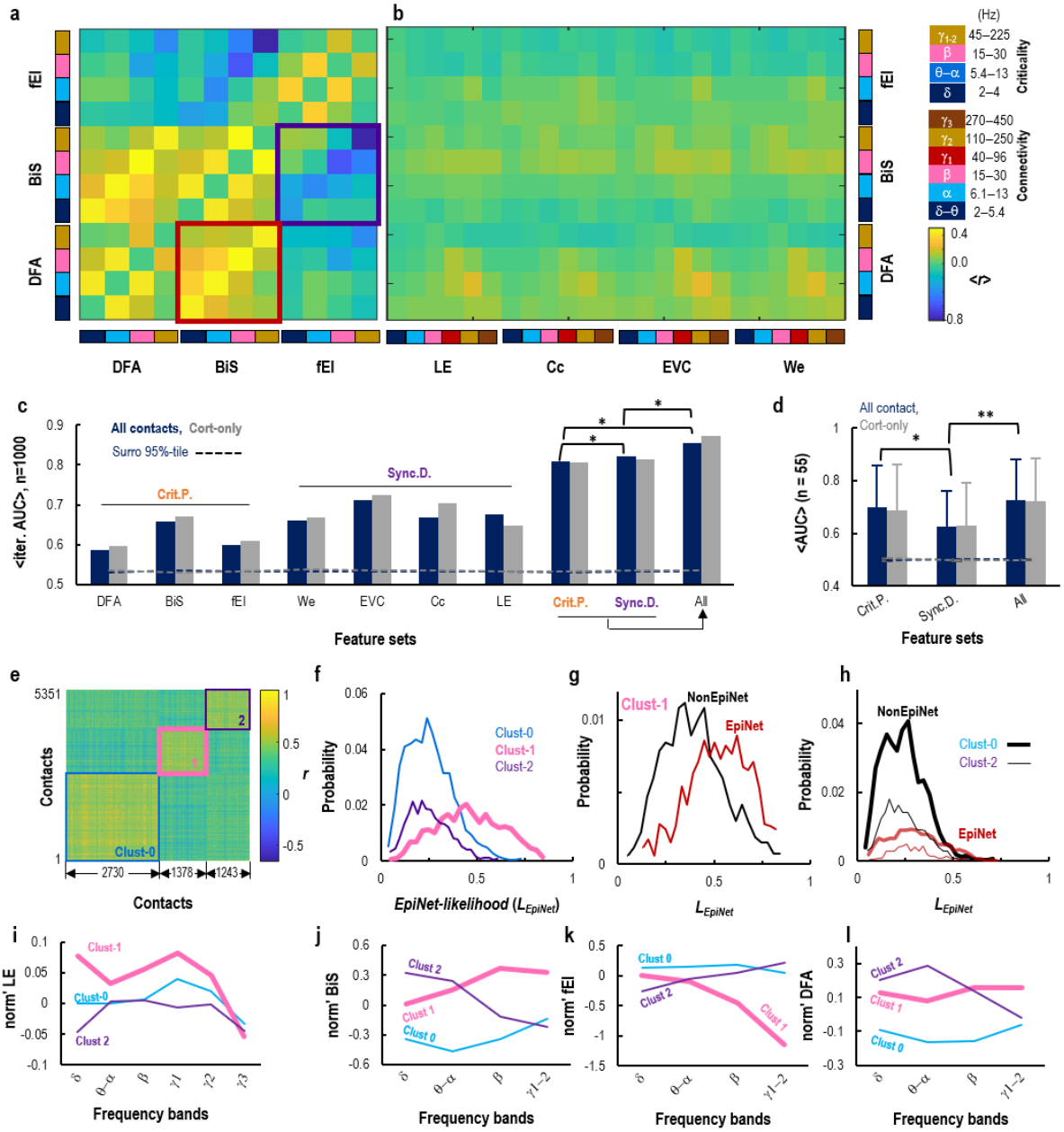

Figure 4: ***Achieving optimal EpiNet classification by combining criticality and synchrony features.*** **a.** Mean with-patient Spearman's correlation ($< r >$) between band-collapsed criticality assessments. **b.** Similarity between criticality and connectivity across frequencies. **c.** Population pooled SEEG contacts classification cross-validation (randomly split $20\% vs 80\%$ test vs train set over 1000 iterations) when using different feature set. AUC: mean area under the receiver-operator-curve; * indicates differences (repeated t-test, $-log10(p)$ in sequence: 62.1, 39.9, 117.8, Benjamini-Hochberg FDR corrected); dashed line: surrogates mean ($n_{surro} = 1000$). **d.** Mean subject AUC (n=55) of within-patient EpiNet-classification; * and **: indicate differences (unpaired t-test, $-log10(p) = 2.2$ and 6.1, respectively (FDR corrected); error bars: standard deviation; dashed lines: surrogate mean ($n_{surro} = 1000$). **e.** All-to-all SEEG contact similarity matrix, and the boxes demarcate three clusters. **f.** Distribution of EpiNet-likelihood (the classifier assess how likely a SEEG contact is an EpiNet) for each contact-cluster defined in (**e**). **g–h.** L_{EpiNet} of EpiNet and NonEpiNet contacts of (**g**) cluster-1, (**h**) cluster-0 and cluster-2. **i–l.** Intra-cluster group average of (**i**) LE , (**j**) BiS, (**k**) fEI, and (**l**) DFA. Inter-cluster differences in theses features see Supplementary Fig 8 (e–f).

References

1. Fisher RS, Cross JH, French JA, et al. Operational classification of seizure types by the International League Against Epilepsy: Position Paper of the ILAE Commission for Classification and Terminology. *Epilepsia.* 2017;58(4):522-530.

2. Devinsky O, Vezzani A, O'Brien TJ, et al. Epilepsy. *Nature Reviews Disease Primers.* 2018;4(May).

3. England M, Liverman C, Schultz A, Strawbridge L. , eds.*Epilepsy Across the Spectrum: Promoting Health and Understanding.* Washington (DC): National Academies Press (US) 2012.

4. DiGiacomo R, Uribe-San-Martin R, Mai R, et al. Stereo-EEG ictal/interictal patterns and underlying pathologies. *Seizure.* 2019;72:54-60.

5. Bartolomei F, Guye M, F W. Abnormal binding and disruption in large scale networks involved in human partial seizures. *EPJ Nonlinear Biomed Phys.* 2013.

6. Luders H, Engel J, Munari C. *General principles. In: Surgical Treatment of the Epilepsies 2nd ed.* New York: Raven Press 1993.

7. Cardinale F, Rizzi M, Vignati E, et al. Stereoelectroencephalography: Retrospective analysis of 742 procedures in a single centre. *Brain.* 2019;142(9):2688–2704.

8. Bulacio JC, Bena J, Suwanpakdee P, et al. Determinants of seizure outcome after resective surgery following stereoelectroencephalography. *Journal of Neurosurgery.* 2022;136(6):1638–1646.

9. Cossu M, Fuschillo D, Casaceli G, et al. Stereoelectroencephalography-guided radiofrequency thermocoagulation in the epileptogenic zone: a retrospective study on 89 cases. *J Neurosurg.* 2015.

10. Lanen RH, Colon AJ, Wiggins CJ, et al. Ultra-high field magnetic resonance imaging in human epilepsy: A systematic review. *NeuroImage: Clinical.* 2021;30:102602.

11. Avigdor T, Abdallah C, Ellenrieder N, et al. Fast oscillations ¿40 Hz localize the epileptogenic zone: An electrical source imaging study using high-density electroencephalography. *Clinical Neurophysiology.* 2021;132.

12. Zweiphenning W, van MA, Klink NEC, et al. Intraoperative electrocorticography using high-frequency oscillations or spikes to tailor epilepsy surgery in the Netherlands (the HFO trial): a randomised, single-blind, adaptive non-inferiority trial. *Articles Lancet Neurol.* 2022;21:982-93.

13. Gnatkovsky V, Curtis MD, Pastori C, et al. Biomarkers of epileptogenic zone defined by quantified stereo-EEG analysis. *Epilepsia.* 2014;55:296-305.

14. Zijlmans M, Zweiphenning W, Klink N. Changing concepts in presurgical assessment for epilepsy surgery. *Nature Reviews Neurology.* 2019;15(10):594–606.

15. Perucca P, Gotman J. Delineating the epileptogenic zone: spikes versus oscillations. *The Lancet Neurology.* 2022;21(11):949–951.

16. Bernabei JM, Li A, Revell YA, et al. Quantitative approaches to guide epilepsy surgery from intracranial EEG. *Brain.* 2023.

17. Thom R. *Structural Stability And Morphogenesis.* Boca Raton: CRC Press1st ed. ed. 1972.

18. Chialvo DR. Emergent complex neural dynamics. *Nature Physics.* 2010;6(10):744–750.

19. Beggs JM. The criticality hypothesis: How local cortical networks might optimize information processing. *Philosophical Transactions of the Royal Society A.* 2008;366:329-343.

20. Linkenkaer-Hansen K, Nikouline VV, Palva JM, Ilmoniemi RJ. Long-Range Temporal Correlations and Scaling Behavior in Human Brain Oscillations. *The Journal of Neuroscience.* 2001;21(4):1370–1377.

21. Bruining H, Hardstone R, Juarez-Martinez EL, et al. Measurement of excitation-inhibition ratio in autism spectrum disorder using critical brain dynamics. *Scientific Reports.* 2020;10(1).

22. Zimmern V. Why Brain Criticality Is Clinically Relevant: A Scoping Review. *Frontiers in Neural Circuits.* 2020;14.

23. Liu X, Ward BD, Binder JR, Li SJ, Hudetz AG. Scale-free functional connectivity of the brain is maintained in anesthetized healthy participants but not in patients with unresponsive wakefulness syndrome. *PLoS ONE.* 2014;9(3).

24. Hobbs JP, Smith JL, Beggs JM. Aberrant neuronal avalanches in cortical tissue removed from juvenile epilepsy patients. *Journal of Clinical Neurophysiology.* 2010;27(6):380–386.

25. Auno S, Lauronen L, Wilenius J, Peltola M, Vanhatalo S, Palva JM. Detrended fluctuation analysis in the presurgical evaluation of parietal lobe epilepsy patients. *Clinical Neurophysiology.* 2021;132.

26. Monto S, Vanhatalo S, Holmes MD, Palva JM. Epileptogenic neocortical networks are revealed by abnormal temporal dynamics in seizure-free subdural EEG. *Cerebral Cortex.* 2007;17(6):1386–1393.

27. Muñoz MA. Colloquium: Criticality and dynamical scaling in living systems. *Reviews of Modern Physics.* 2018;90(3).

28. Wilson HR, Cowan JD. Excitatory and Inhibitory Interactions in Localized Populations of Model Neurons. *Biophysical Journal.* 1972;12(1):1–24.

29. Freyer F, Roberts JA, Ritter P, Breakspear M. A Canonical Model of Multistability and Scale-Invariance in Biological Systems. *PLoS Computational Biology.* 2012.

30. Steriade M, Nunez A, Amzica F. A novel slow (¡ 1 Hz) oscillation of neocortical neurons in vivo: Depolarizing and hyperpolarizing components. *Journal of Neuroscience.* 1993;13(8):3252–3265.

31. Holcman D, Tsodyks M. The emergence of Up and Down states in cortical networks. *PLoS Computational Biology.* 2005;preprint(2006):e23.

32. Freyer F, Aquino K, Robinson PA, Ritter P, Breakspear M. Bistability and Non-Gaussian Fluctuations in Spontaneous Cortical Activity. *Journal of Neuroscience.* 2009.

33. Freyer F, Roberts JA, Becker R, Robinson PA, Ritter P, Breakspear M. Biophysical Mechanisms of Multistability in Resting-State Cortical Rhythms. *Journal of Neuroscience.* 2011.

34. Wang SH, Arnulfo G, Myrov V, et al. Critical-like bistable dynamics in the resting-state human brain. *bioRxiv.* 2022:2022.01.09.475554.

35. Buendía V, Santo S, Bonachela JA, Muñoz MA. Feedback Mechanisms for Self-Organization to the Edge of a Phase Transition. 2020.

36. Santo S, Villegas P, Burioni R, Muñoz MA. Landau–Ginzburg theory of cortex dynamics: Scale-free avalanches emerge at the edge of synchronization. *Proceedings of the National Academy of Sciences.* 2018;115(7):E1356–E1365.

37. Anderson PW. More Is Different. *Science.* 1972;177(4047):393–396.

38. Fries P. A mechanism for cognitive dynamics: Neuronal communication through neuronal coherence. *Trends in Cognitive Sciences.* 2005;9(10):474–480.

39. Singer W. Neuronal synchrony: a versatile code for the definition of relations?. *Neuron.* 1999;24:49–65.

40. Fuscà M, Siebenhühner F, Wang SH, et al. Brain criticality predicts individual synchronization levels in humans. *bioRxiv.* 2022.

41. Bullmore E, Sporns O. The economy of brain network organization. *Nature Reviews Neuroscience.* 2012;13:336–349.

42. Gunnarsdottir KM, Li A, Smith RJ, et al. Source-sink connectivity: a novel interictal EEG marker for seizure localization. *Brain : a journal of neurology.* 2022;145(11):3901–3915.

43. Gupta K, Grover P, Abel TJ. Current Conceptual Understanding of the Epileptogenic Network From Stereoelectroencephalography-Based Connectivity Inferences. *Frontiers in Neurology.* 2020;11(November):1–7.

44. Friston KJ. Functional and Effective Connectivity: A Review. *Brain Connectivity.* 2011;1(1):13–36.

45. Bullmore E, Sporns O. Complex brain networks: Graph theoretical analysis of structural and functional systems. 2009.

46. Rubinov M, Sporns O. Complex network measures of brain connectivity: Uses and interpretations. *NeuroImage.* 2010;52(3):1059–1069.

47. Khambhati AN, Davis KA, Oommen BS, et al. Dynamic Network Drivers of Seizure Generation, Propagation and Termination in Human Neocortical Epilepsy. *PLoS Computational Biology.* 2015;11(12):1–19.

48. Arnulfo G, Hirvonen J, Nobili L, Palva S, Palva JM. Phase and amplitude correlations in resting-state activity in human stereotactical EEG recordings. *NeuroImage.* 2015:114–127.

49. Fischl B, Salat D, Busa E, et al. Neurotechnique Whole Brain Segmentation: Automated Labeling of Neuroanatomical Structures in the Human Brain. *Neuron.* 2002;33:341–355.

50. Arnulfo G, Narizzano M, Cardinale F, Fato MM, Palva JM. Automatic segmentation of deep intracerebral electrodes in computed tomography scans. *BMC Bioinformatics.* 2015;16(1).

51. Proix T, Bartolomei F, Guye M, Jirsa V. Individual brain structure and modelling predict seizure propagation. *Brain.* 2017.

52. Lara Jehi . The Epileptogenic Zone: Concept and Definition. *Epilepsy Currents.* 2018;18(1):12–16.

53. Arnulfo G, Wang S, Myrov V, et al. Long-range phase synchronization of high-frequency oscillations in human cortex. *Nature Communications.* 2020;11(1).

54. Lundberg SM, Allen PG, Lee SI. A Unified Approach to Interpreting Model Predictions. in *Conference on Neural Information Processing Systems (NIPS) 31st*(Long Beach) 2017.

55. Breiman L. Random Forests. in *Machine Learning*;45:5–32Kluwer Academic Publishers 2001.

56. Sokal RR, Michener CD. A statistical method for evaluating systematic relationships. *University of Kansas science bulletin.* 1958;38:1409-1438.

57. Nobili L, Proserpio P, Combi R, et al. Nocturnal frontal lobe epilepsy. *Current Neurology and Neuroscience Reports.* 2014;14(2).

58. Martín PV, Bonachela JA, Levin SA, Muñoz MA. Eluding catastrophic shifts. *Proceedings of the National Academy of Sciences.* 2015;112:E1828-E1836.

59. Cowan JD, Neuman J, Drongelen W. Wilson–Cowan Equations for Neocortical Dynamics. *Journal of Mathematical Neuroscience.* 2016;6:1-24.

60. Rho JM, Boison D. The metabolic basis of epilepsy. *Nature Reviews Neurology.* 2022;18:333-347.

61. McDonald T, Puchowicz M, Borges K. Impairments in oxidative glucose metabolism in epilepsy and metabolic treatments thereof. *Frontiers in Cellular Neuroscience.* 2018;12.

62. Vezzani A, French J, Bartfai T, Baram TZ. The role of inflammation in epilepsy. *Nature Reviews Neurology.* 2011;7.

63. Vezzani A, Balosso S, Ravizza T. Neuroinflammatory pathways as treatment targets and biomarkers in epilepsy. *Nature Reviews Neurology.* 2019;15.

64. Beenhakker MP, Huguenard JR. Neurons that Fire Together Also Conspire Together: Is Normal Sleep Circuitry Hijacked to Generate Epilepsy?. *Neuron.* 2009;62:612-632.

65. Karoly PJ, Rao VR, Gregg NM, et al. Cycles in epilepsy. *Nature Reviews Neurology.* 2021;17:267-284.

66. Jirsa VK, Stacey WC, Quilichini PP, Ivanov AI, Bernard C. On the nature of seizure dynamics. *Brain.* 2014.

67. Li A, Huynh C, Fitzgerald Z, et al. Neural fragility as an EEG marker of the seizure onset zone. *Nature Neuroscience.* 2021;24:1465-1474.

68. Fisher RS, Scharfman HE, DeCurtis M. How Can We Identify Ictal and Interictal Abnormal Activity?. *Adv Exp Med Biol.* 2014:3–23.

69. Critical slowing down as a biomarker for seizure susceptibility. *Nature Communications.* 2020;11(1):1–12.

70. Breakspear M, Heitmann S, Daffertshofer A. Generative Models of Cortical Oscillations: Neurobiological Implications of the Kuramoto Model. *Frontiers in Human Neuroscience.* 2010.

71. Hardstone R, Poil SS, Schiavone G, et al. Detrended fluctuation analysis: A scale-free view on neuronal oscillations. *Frontiers in Physiology.* 2012.

72. Lachaux JP, Rodriguez E, Martinerie J, Varela FJ. Measuring Phase Synchrony in Brain Signals. *Hum Brain Mapping.* 1999;8:194–208.

A Supplementary materials

A.1 Supplementary methods

A.1.1 The bistability in Thom's cusp catastrophe

Catastrophes emerging from complex systems are characterized by sudden and violent onsets, detrimental consequences, and are suggested to be generated by only few candidate mechanisms [17]. We suggest the emergence of epileptic hypersynchrony in neuronal population to be explain by Thom's cusp catastrophe:

$$V(R, a, b) = R^4 + aR^2 + bR \tag{1}$$

where R is synchrony; the stable solution for the potential function satisfies V:

$$\frac{\delta V}{\delta R} = R^3 - aR - b = 0 \tag{2}$$

which defines the cusp fold, wherein the attractor of R, *e.g.*, experimentally observed mean synchrony over time, is controlled by two parameters: a modulates the degree of R, *e.g.*, a large a results in hypersynchrony; as b increases, bistability in R gradually emerges (Fig 1). High bistability invariably predicts catastrophic events across a wide array of complex systems (reviewed in [34]), and likely is the underlying bifurcation mechanism for epileptic seizures.

A.1.2 Catastrophic hypersynchrony in a modified Kuramoto model

We built a modified Kuramoto model based on the classic definition [70] to investigate the catastrophic hypersynchrony in neuronal oscillation dynamics. The theory and motivation of the model were discussed in [34]. Briefly, we introduced a state-dependent noise to this Kuramoto model to reflect the local-positive feedback, and the dynamics of each oscillator i of the model is a scalar phase time series $\theta_i(\theta \in 0 : 2\pi)$ coupled into the model ensemble θ as,

$$\dot{\theta}_i = \omega_i + K_i + Z_i \tag{3}$$

where, $\omega_i = 11$ Hz is the natural frequency of the oscillators; K_i is the coupling between oscillators and the Z_i is the state-dependent noise. The coupling function $K_i(\theta)$ can be interpreted as oscillator i adjusts its phase due to the interaction with all other oscillators in the model and is defined as:

$$K_i = \frac{a}{N}\sum_{n=1}^{N} sin(\theta_i - \theta_j) \tag{4}$$

where a is the coupling strength between oscillators (Fig 1); $N = 200$ is the number of oscillators that are all-to-all connected in the model. The noise Z_i is defined as:

$$Z_i = \eta[1 - b]\zeta_a(t) + b(R_{MAX} - R)\zeta_m(t) \tag{5}$$

where $\zeta_a(t)$ and $\zeta_m(t)$ represent additive and multiplicative noise, respectively, and they are two independent Gaussian time series with zero mean and unit variance; the strength of positive local feedback b scales the influence of $\zeta_m(t)$ depending on the current level of synchrony R; $R_{MAX} = 1$ is the maximal synchrony the population can reach, and the order parameter R, aka the synchrony among all the oscillators, is defined as:

$$R(t) = \left| \frac{1}{n}\sum_{n=1}^{N}[e^{i\theta_n(t)}] \right| \tag{6}$$

hence when the population is in full synchrony, $R \to 1$; when the population is fully desynchronized, $R \to 0$.

A.1.3 Criticality assessments

Assessing neuronal bistability with the BiS index. We used the BiS index to assess the bistability of a power time series (R^2). Briefly, we followed the approach proposed in [32, 33] to obtain the probability distribution function (*pdf*) of a narrow-band power time series R^2 with 200 bins. Next, because the square of a Gaussian process has an exponential *pdf*, we used maximum likelihood estimate (MLE) to fit the observed *pdf* with a single-exponential function:

$$P_{R^2}(R^2) = \gamma e^{-\gamma R^2} \tag{7}$$

next, the same *pdf* was fitted with a bi-exponential function:

$$P_{R^2}(R^2) = \delta\gamma_1 e^{-\gamma_1 R^2} - (1-\delta)\gamma_2 e^{-\gamma_2 R^2} \tag{8}$$

where where γ_1, γ_2 are the two exponents and δ is a weighting factor. Next, we used the Bayesian information criterion (BIC) to assess the fitting of eq.7 and eq.8:

$$BIC = ln(n)k - 2ln(\hat{L}) \tag{9}$$

where, n is sample number; $\hat{L}$ is the likelihood function; k is the number of parameters, i.e., for eq.7, $k = 1$ and for eq.8 and $k = 3$. A better fitted model yields a small BIC estimate. Hence, the BIC imposes a penalty to model complexity of eq.8 for two more degrees of freedom than eq.7. Finally, the BiS index is computed as the log_{10} transform of the difference between the BIC of the two models $dBIC = BIC_{singleExp} - BIC_{biExp}$ as :

$$BiS = log_{10}(dBIC),\ if\ dBIC > 0; \qquad BiS = 0, if\ dBIC \leq 0 \tag{10}$$

because a better fitted model yields a small BIC estimate, the BiS will be large if the bi-exponential model is a better model for the observed *pdf* of the oscillation power time series.

Assessing neuronal LRTCs using the DFA. We followed the approach proposed by [20] to assess the LRTCs of the narrow-band oscillation amplitudes with linear detrend fluctuation analysis (DFA). The theory, technical details, and the toolbox of the DFA are well described in [71]. Briefly, an estimated DFA exponent reflects the finite-size power-law scaling in narrow-band amplitude fluctuations based on the assumption that the gradual evolution of a mono-fractal time series would result in a normal distribution where the fluctuations can be captured by the second order statistical moments. In practice, DFA characterizes how fast the overall root mean square of local detrend fluctuations F grows with increasing sampling window size L:

$$F(L) = CL^{\beta} \tag{11}$$

where C is a constant; β is the DFA exponent and $\beta > 0.6$ can be safely considered as a sign of a critical-like process, e.g., significantly greater than that of a random walk process ($DFA = 0.5$, see Fig 2 and Supplementary Fig 4 for fitting examples). Here, for assessing narrow-band amplitude DFA, we set L as 40 windows with their size ranging from 20-cycle length (*e.g.*, 2 seconds for 10 Hz) to 2.5 min with equal *log* distance between windows; the $F(L_i)$ were computed for a given window size L_i as the mean of the root mean square of the detrend fluctuation with 50% overlap between neighbouring windows, and a window was excluded from the mean if more than 10% of its samples contain interictal events; the linear regression of eq.11 was done with a bi-square fitting weighted by the square root of observed window number for a given L_i.

Assessing neuronal excitation-inhibition with the fEI. We followed the approach proposed by [21] to assess the functional excitation/inhibition (E/I) of a narrow-band oscillation amplitudes with the fEI index:

$$fEI = 1 - r(w_{amp}, w_{nF(t)}) \tag{12}$$

where w_{amp} denotes observed windowed oscillation amplitudes; $w_{nF(t)}$ is the observed windowed detrend function of the amplitude-normalized signal profiles; $r(w_{amp}, w_{nF(t)})$ denotes the Pearson's correlation between $w_{amp}, w_{nF(t)}$. Thus, based on Bruining's hypothesis that, if a time series is generated by a critical-like mechanism, we expect to observe, for an inhibition-dominated ensemble $fEI < 1$; for an excitation-dominated ensemble $fEI > 1$, and for an E/I balanced ensemble $fEI = 1$ (illustrated in Supplementary Fig 2 j). Here, for assessing narrow-band amplitude fEI, we set window size as 50-cycle length (*e.g.*, 5 seconds for 10 Hz) with 60% overlap between windows.

A.1.4 Phase synchrony assessment

The phase coupling between two narrow-band time series A and B (complex-valued) can be quantified as the phase-locking value as [72]:

$$PLV = |cPLV(A,B)| = \left| \frac{1}{T} \sum_{t=1}^{T} [e^{i(\theta_A(t) - \theta_B(t))}] \right| \tag{13}$$

where T denotes the total number of independent samples; θ_A and θ_B are the instantaneous phases of A and B. We denote a PLV connectivity matrix as a "graph" $G_{iPLV} = (V, E)$, where any SEEG contact i is a "node" $v_i \in V$; the PLV between two nodes (v_i, v_j) are edges, $e_k = (v_i, v_j) \in E | v_i, v_i \in V$. The first- and second-order synchrony derivatives were computed using these PLV matrices.

A.2 Supplementary results

A.2.1 Synchrony derivatives (Synch.D) were robust against various random attacks

The anatomical coverage and number of SEEG contacts were variable across subjects. Moreover, some PLV edges were excluded from analyses if two contacts shared the same white-matter reference [48]. This raised a slight concern about whether the spatial sampling variability and missing edges in the PLV matrices would bias the first- and second-order Synch.D. Hence, we conducted random deletions to the edges and to the nodes in graphs and then compared Synch.D before and after the deletions to ask whether synchrony derivatives were resilient against these varying factors. This was done by computing the Pearson's correlation r between the synchrony derivatives between the original and assaulted graphs, and as $r \to 1$ means that the nodal topological features were preserved after the assault. Additionally, these Synch.D estimates were computed with weighted PLV graphs would be different after removing edges or nodes; in the EpiNet-classification analyses, we normalized synchrony derivatives within subjects, and therefore different estimates was not a concern here.

After the shared-reference exclusion, subjects' PLV graph density was $0.92 \pm 0.04 (mean \pm std, range: 0.81 - 0.96)$, where one means a fully connected network without nodal self-connection. To ascertain that the missing edges did not significantly impact the synchrony derivatives, we performed population-level edge deletion tests. We took 4.8 Hz PLV matrices from the 55 patients of the EpiNet-classification cohort. We next assaulted each subject's PLV matrix by randomly deleting $x\%$ of edges in one surrogate run, and then compute the Pearson's r between the Synch.D between the nodes from the original and assaulted graphs. We conducted 500 of such surrogates within each patient and across edge deletion ratio $x\% \in [10:10:90, 91:1:98]$, which assured that all synchrony derivatives (*i.e.*, We, EVC, Cc, and LE) were resilient to random edge deletion – specifically for the range of the missing data observed (Supplementary Fig 4 **a, c**).

Next, to ascertain that heterogeneity in SEEG spatial sampling or sub-sampling the targeted network did not significantly impact the synchrony derivatives, we performed population-level nodal removal tests. We used 4.8 Hz PLV matrices from the 55 patients and assaulted each subject's PLV matrix by randomly removing $y\%$ of nodes in one surrogate run, and then compute the Pearson's r between the synchrony derivatives of the remaining nodes from the assaulted and the original graphs. We conducted 500 of such surrogates within each patient and across nodal removal ratio $y\% \in [10:10:90, 91:1:95]$, which assured that all synchrony derivatives (*i.e.*, We, EVC, Cc, and LE) were resilient to random nodal removal (Supplementary Fig 4 **b, d**).

A.2.2 Supervised EpiNet-Classification

The individual variability in EpiNet-classification outcomes can be explained by several factors. Individual area under (AUC) the receiver operator characteristic curve was negatively correlated with the standard deviation of edge-distance (Spearman's rank $r = -0.3$, $p < 0.026$), but was not correlated with mean edge distance (Spearman's rank $r = -0.24$, $p > 0.076$) nor total number of edges (Spearman's $r = -0.23$, $p > 0.091$), which means relatively concentrated spatial sampling rather than the spatial extent of the spatial sampling helps with increasing individual AUC. The L_{EpiNet} ($0-100\%$, *i.e.*, the likelihood of being an EpiNet contact) assigned by the random-forest were different between the EpiNet and NonEpiNet contacts (unpaired t-test, $p < 6.8 \times 10^{-157}$), and the difference in EpiNet and NonEpiNet contacts' EpiNet-likelihood predicted patient AUC (Spearman's rank $r = 0.93$, $p < 10^{-6}$, Supplementary Fig 7 k).

A.3 Supplementary Figures

A.3.1 Supplementary Fig 1

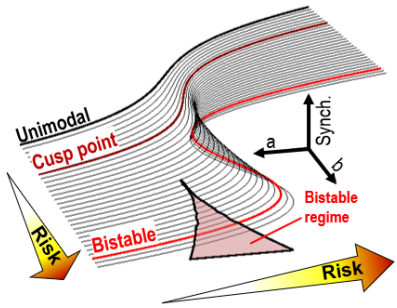

Figure 1: **The cusp catastrophe offers a canonical explanation to the link between high bistability and catastrophic neuronal hypersynchrony.** On the cusp fold, each point along the curve indicates the stable solution of R with a given pair of a and b; a large R corresponding to seizure-like hypersynchrony, and as b increases, the curves shifts shape from smooth to discontinuous transition in the temporal dynamics of R.

A.3.2 Supplementary Fig 2

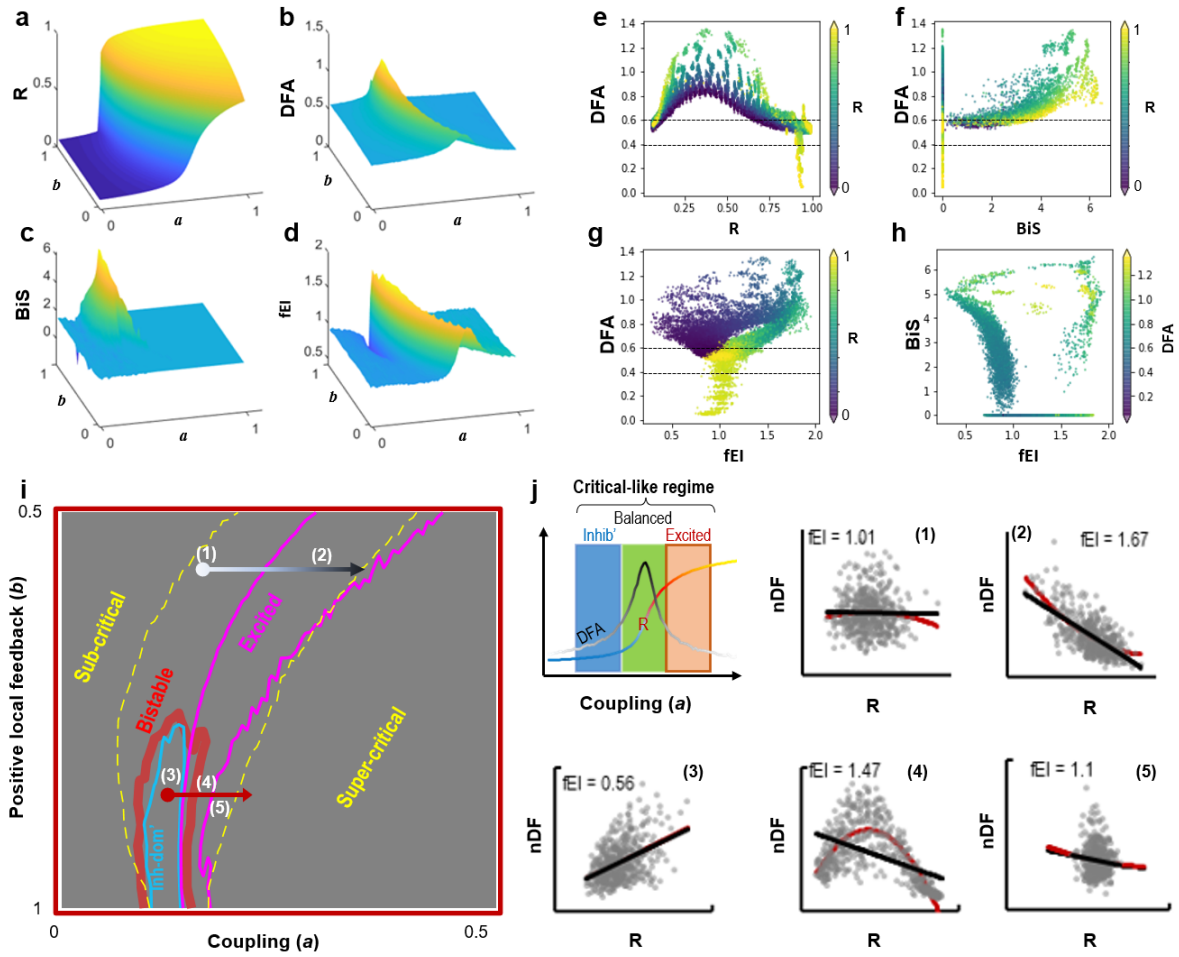

Figure 2: **High bistability in neuronal synchrony of the model indicates a shift toward catastrophic hypersynchrony. a–d.** Assessments averaged over 20 independent model realization for **(a)** model synchrony (R), **(b)** DFA exponent **(c)** BiS index and **(d)** fEI index. **e–h.** Co-variability between the criticality assessments. **i.** In high bistability regime, a small increment in a (red vector) could drive the model from adaptive critical-like dynamics into seizure-like hypersynchrony, during which the model can show radical switching from inhibition-dominance (3) to excitation-dominance (4). **j.** Schematic showing how the fEI index utilizes distinct relationship between R and nDF (normalized detrend function) to capture the model operation dynamics in three regions inside critical regime. Inhib': inhibition-dominance; excited: excitation-dominance; (1–5) the functional excitation-inhibition as response to a increment inside and outside of the bistable regime (as marked in (**i**)), each marker indicates the estimates of an analysis window of 1000 samples; also note that data can sometimes be fitted with a quadratic function indicating a wider operation region than one of the three regions.

A.3.3 Supplementary Fig 3

Figure 3: **SEEG contacts from both EpiNet and NonEpiNet can show bistable activity. a–b.** Broad-band traces and narrow-band power time series showing that higher bistability in an EpiNet than in a nearby NonEpiNet contact locations in two subjects. **c.** NonEpiNet contacts can also demonstrate bistability as shown here in 4 and 80 Hz narrow-band oscillations from another two subjects.

A.3.4 Supplementary Fig 4

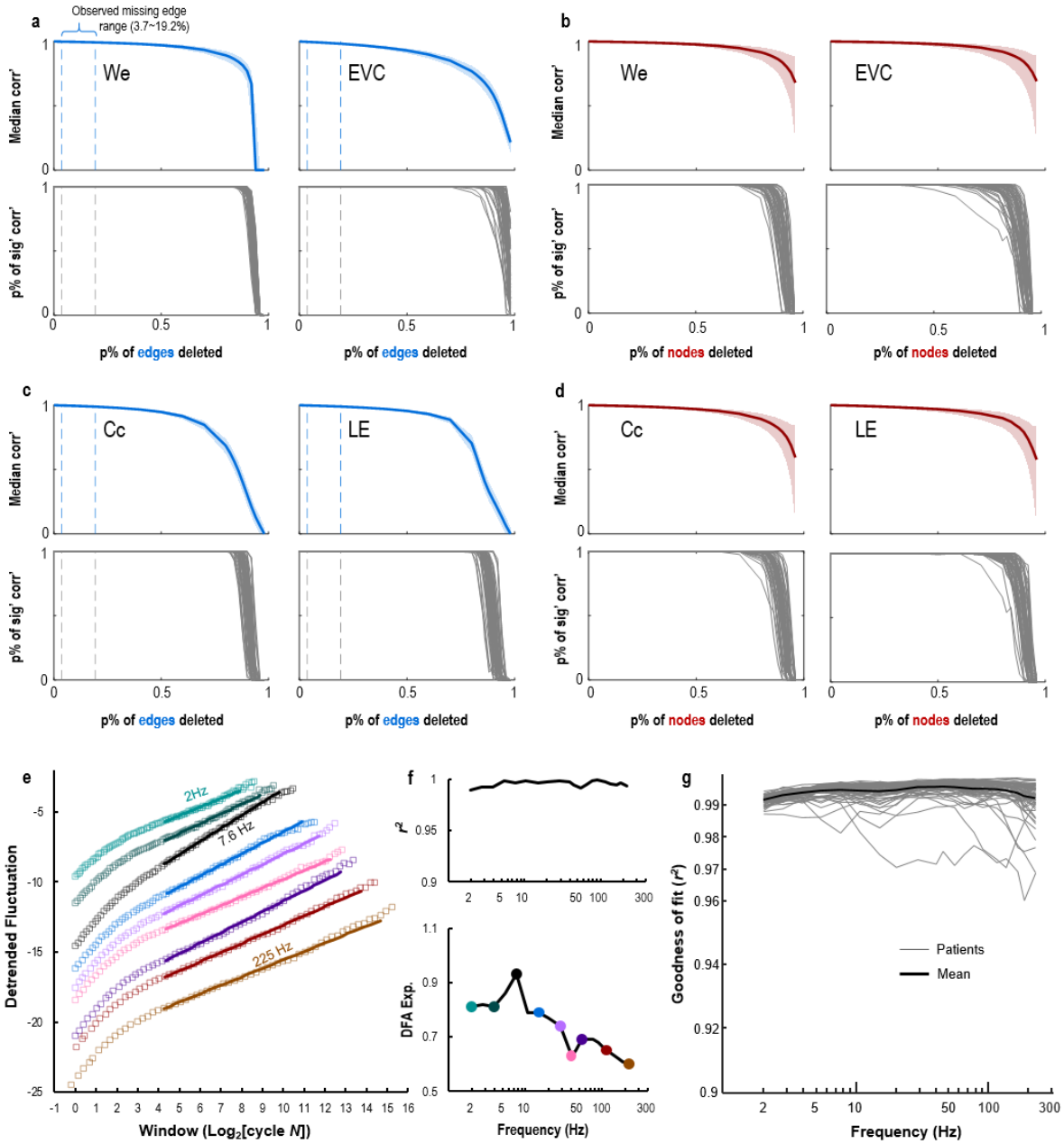

Figure 4: **Synchrony derivatives were resilient against random attacks and DFA goodness-of-fit was consistent across frequencies and subjects . a–b.** The first- and **(c–d)** second-order synchrony derivatives (Synch.D) employed in EpiNet-classification were highly resilient to random edge deletion (blue) or nodal removal (red). ***Top:*** median correlation (Pearson's r) between the Synch.D of the original PLV graphs and the graphs under increasing levels of random assaults, computed over 500 iterations per subject for 55 subjects of the EpiNet-classification cohort; shaded areas indicate interquartile distance. ***Bottom***: corresponding percent of significant correlations ($p < 0.01$, FDR corrected) out of the 500 surrogates in each subject (thin lines). **e.** An example of how DFA fitting was done across narrow-band frequencies from a SEEG contact of a randomly selected subject. Markers indicate observed data. Lines indicate DFA linear fitting, and the fitting range was from 20 cycle-length of a given narrow-band frequency up to 25% of the 10-min resting-state recording. **f.** ***Top***: goodness of fit (r^2) and ***bottom***: the DFA exponents of the contact from (e). **g.** DFA goodness-of-fit of individual patients' mean across contacts (thin) and group mean (thick).

A.3.5 Supplementary Fig 5

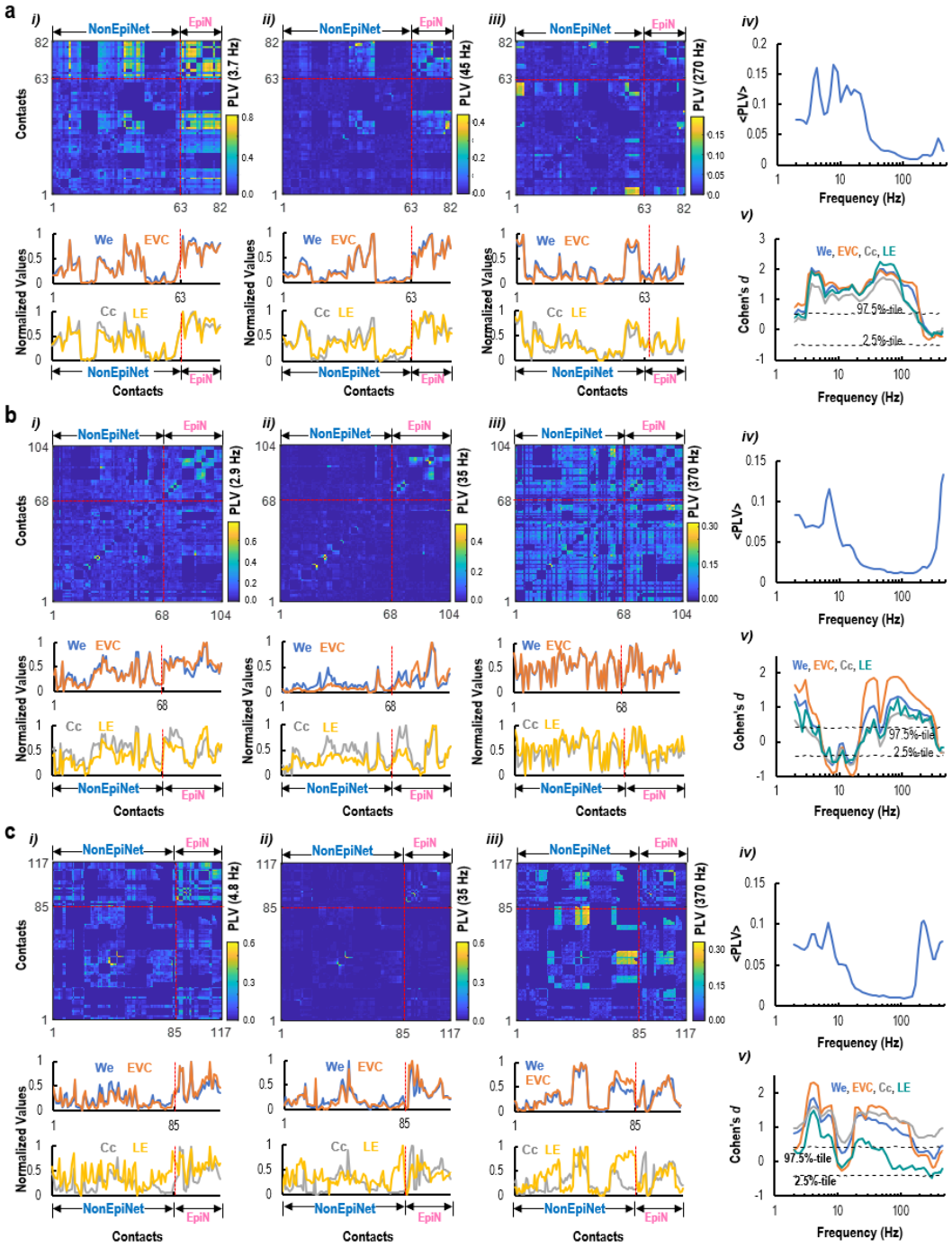

Figure 5: **Individual level evidence of differences between EpiNet and NonEpiNet in synchrony derivatives. a–c.** The narrow-band frequency PLV matrices and their synchrony derivatives (Synch.D), and individual level differences between EpiNet and NonEpiNet in three subjects. Within subjects: ***i-iii***) ***Top***: narrow-band PLV matrices; ***bottom***: We and EVC (first-order) and Cc and LE (second-order Synch.D) of the corresponding PLV matrices. ***iv***) Individual connectivity spectrum, *i.e.*, effective mean PLV edges across narrow-band frequencies. ***v***) Differences between EpiNet and NonEpiNet in Synch.D.

A.3.6 Supplementary Fig 6

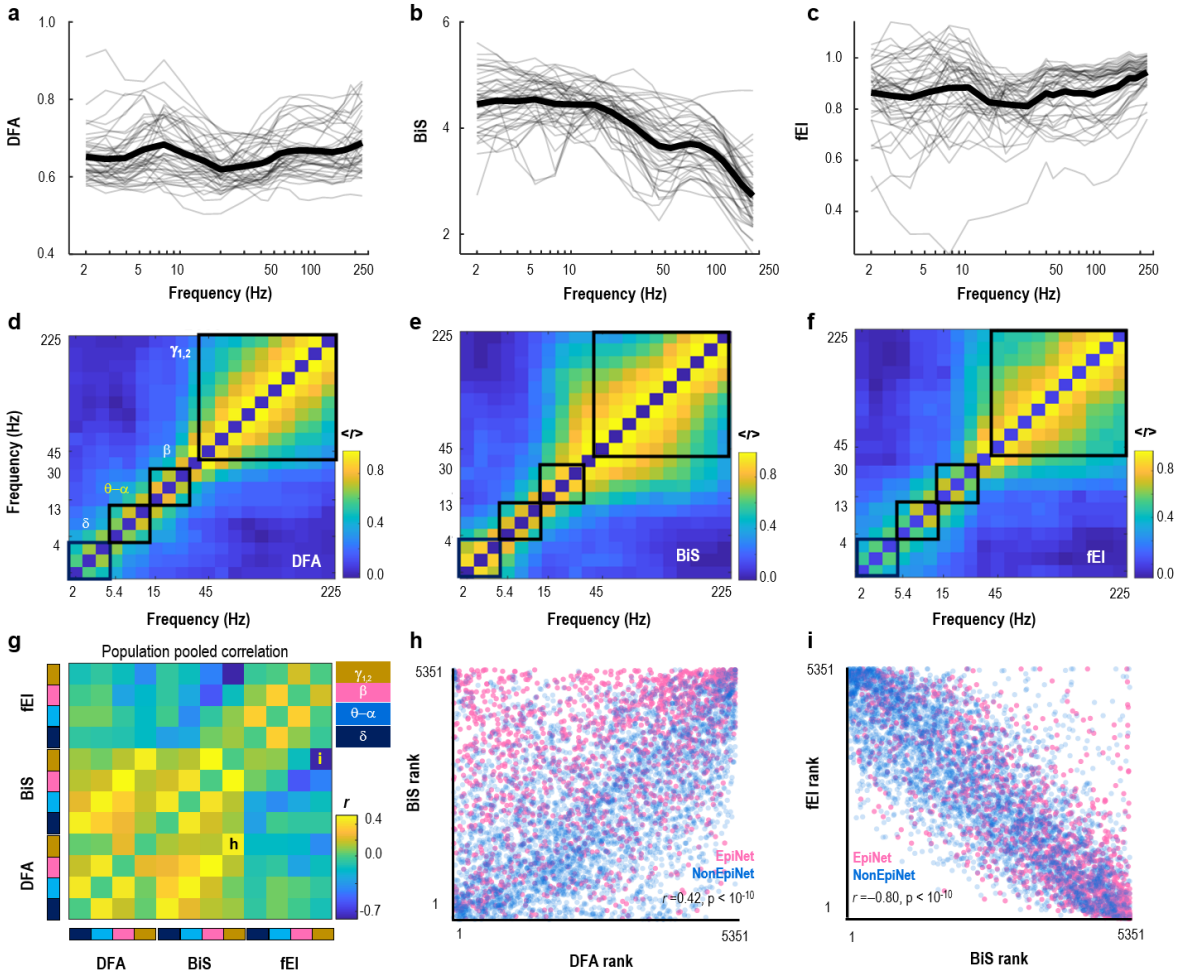

Figure 6: **Supplementary information for frequency clustering by topological similarity. a–c** Within patient mean (thin) and cohort average (thick) (**a**) DFA , (**b**) BiS, and (**c**) fEI. **d–f** Cross-frequency topological similarity (Spearman's rank r) for (**d**) DFA , (**e**) BiS, and (**f**) fEI. **g.** Population pooled Spearman's rank r between frequency clustered criticality assessments (validation for Fig 4 a), **h–i.** Example of the relationship between the Pearson's rank of contact **(h)** $\gamma_{1,2}$ band DFA and BiS estimates, and **(i)** $\gamma_{1,2}$ band BiS and fEI estimates, as indicated in **(g)**.

A.3.7 Supplementary Fig 7

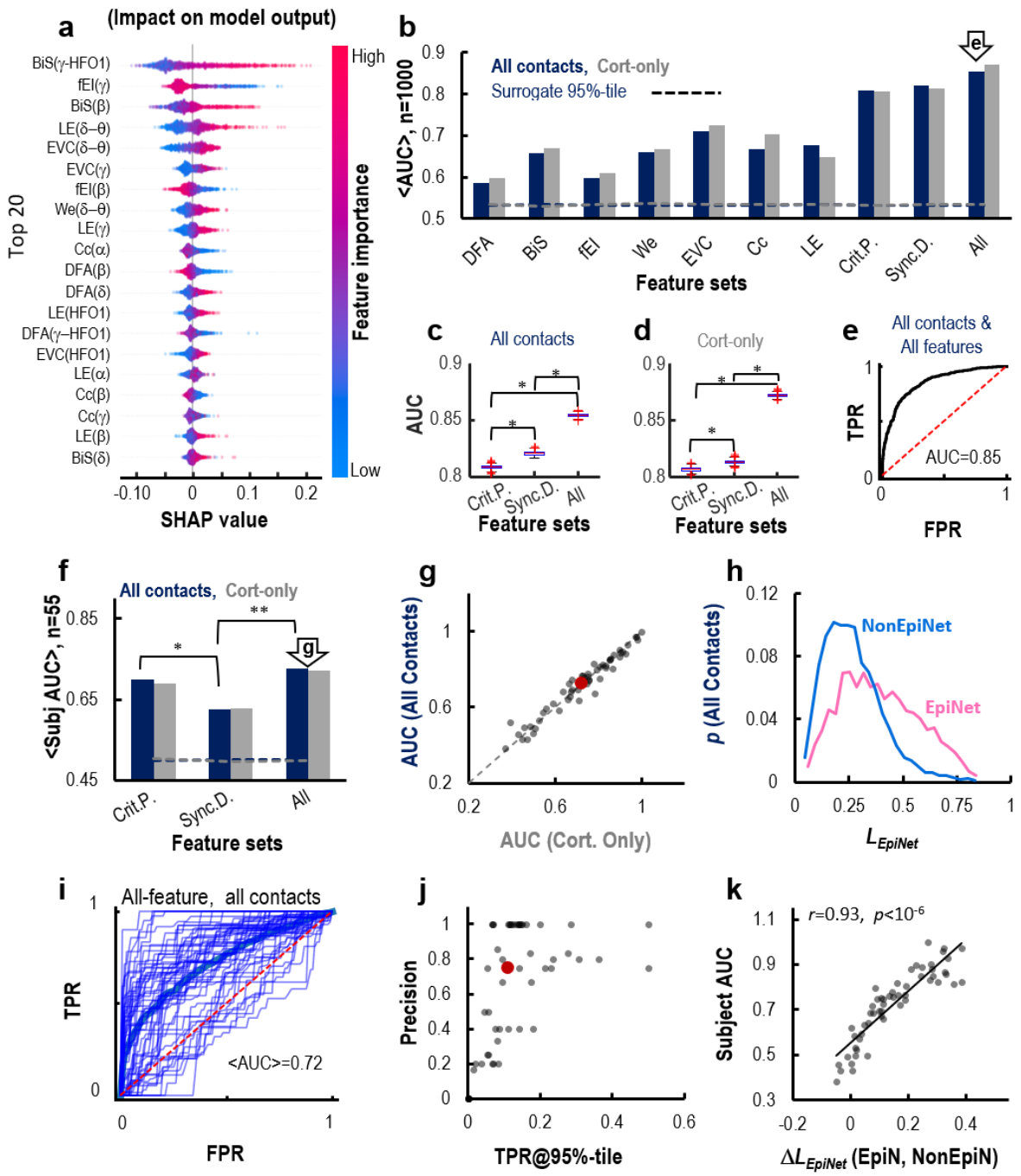

Figure 7: **Supplementary information for the supervised EpiNet-classification (random-forest). a.** Importance ranking of the individual features. **b–d.** Cohort level cross-validate: the support information for Fig 4c. **b.** Difference in area under (AUC) the receiver operating characteristic (ROC) curve for EpiNet-classification using all cortical and subcortical contacts and using **c.** cortical contacts only. **d.** The ROC of a randomly selected EpiNet-classification iteration when using "all features" and "all contacts". **e–h.** Support information for within-patient EpiNet-classification, Fig 4d. **e.** Individual (thin) and group mean ROC curves. **f.** Individual (markers) area under the ROC curve yielded using "all features" and when using all contacts and cortical contacts only. Red marker indicates the mean. **g.** Precision as a function of true positive rate (TRP) when L_{EpiNet} threshold was held at 95% confidence interval for EpiNet-classification using all features and all contacts. **h.** The individual AUC as a function of the difference in L_{EpiNet} between EpiNet and NonEpiNet contacts.

A.3.8 Supplementary Fig 8

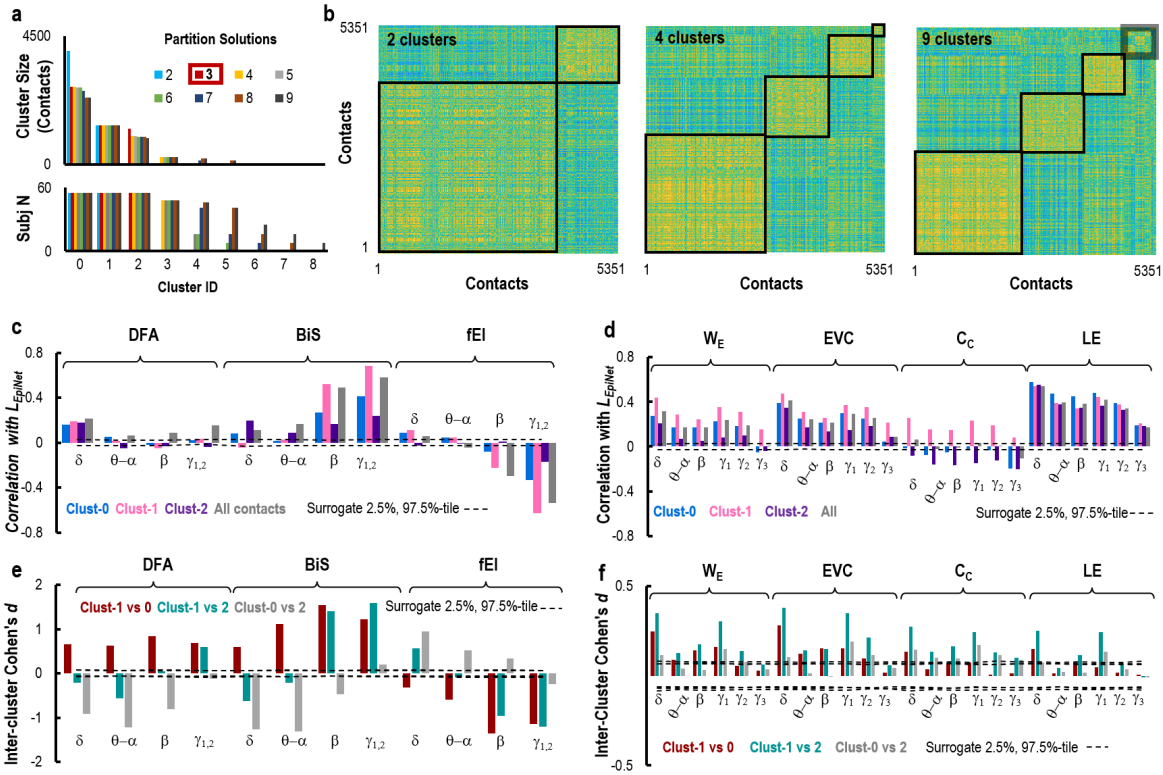

Figure 8: **Supplementary information for unsupervised classification (Fig 4 e–i). a.** Top: cluster size distribution; bottom: distinct subject number within each cluster across partition solution from 2 to 9 clusters color-coded. The 3-cluster solution was used in (Fig 4 e–i). **b.** Visualized partition solutions of the inter-contact similarity (Spearman's rank r) matrix for 2-, 4-, and 9-cluster solutions. The gray box in the 9-cluster solution contains 6 small clusters **c–d.** For the 3-cluster solution: the correlations between the L_{EpiNet}(supervised classifier prediction) and cluster-specific contacts' **c.** criticality assessments and **d.** Support information for statistical tests for (Fig 4 i–l): synchrony derivatives. **e–f.** Statistical tests for (Fig 4 i–l): the inter-cluster contact difference in **e.** criticality assessments and **f.** synchrony derivatives. Dashed lines indicate confidence intervals ($\alpha < 0.05$) observed from 10^4 label-shuffled surrogates.